









Experimental and numerical study on the inertial migration of hydrogel particles suspended in square channel flows

Yuma Hirohata¹ , Kazusa Sai², Yuki Tange², Tomohiro Nishiyama²,
Haruka Minato^{3,4} , Daisuke Suzuki^{3,4} , Tomoaki Itano² ,
Kazuyasu Sugiyama^{1,5}  and Masako Sugihara-Seki² 

¹Graduate School of Engineering Science, The University of Osaka, Toyonaka, Osaka 560-8531, Japan

²Department of Pure and Applied Physics, Kansai University, Suita, Osaka 564-8680, Japan

³Graduate School of Textile Science & Technology, Shinshu University, Ueda, Nagano 386-8567, Japan

⁴Graduate School of Environmental Life Natural Science and Technology, Okayama University,
3-1-1 Tsushimanaka, Kita-ku, Okayama 700-8530, Japan

⁵RIKEN, Wako, 2-1 Hirosawa, Saitama 351-0198, Japan

Corresponding author: Yuma Hirohata, yuma.hirohata@flow.me.es.osaka-u.ac.jp

(Received 21 April 2025; revised 16 July 2025; accepted 11 August 2025)

The inertial migration of hydrogel particles suspended in a Newtonian fluid flowing through a square channel is studied both experimentally and numerically. Experimental results demonstrate significant differences in the focusing positions of the deformable and rigid particles, highlighting the role of particle deformability in inertial migration. At low Reynolds numbers (Re), hydrogel particles migrate towards the centre of the channel cross-section, whereas the rigid spheres exhibit negligible lateral motion. At finite Re , they focus at four points along the diagonals in the downstream cross-section, in contrast to the rigid particles which focus near the centre of the channel face at similar Re . Numerical simulations using viscous hyperelastic particles as a model for hydrogel particles reproduced the experimental results for the particle distribution with an appropriate Young's modulus of the hyperelastic particles. Further numerical simulations over a broader range of Re and the capillary number (Ca) reveal various focusing patterns of the particles in the channel cross-section. The phase transitions between them are discussed in terms of the inertial lift and the lift due to particle deformation, which would act in the direction towards lower shear. The stability of the channel centre is analysed using an asymptotic expansion approach to the migration force at low Re and Ca . The theoretical analysis predicts the critical condition for the transition, which is consistent

with the direct numerical simulation. These experimental, numerical and theoretical results contribute to a deeper understanding of inertial migration of deformable particles.

Key words: flow-structure interactions, microfluidics, particle/fluid flow

1. Introduction

Deformable particles, such as fluid drops, elastic particles, capsules, vesicles and red blood cells, suspended in channel flows have long been known to migrate away from the channel wall at low Reynolds numbers (Re), with few exceptions for fluid drops with a certain range of the viscosity ratio (Karnis, Goldsmith & Mason 1963; Goldsmith 1971; Leal 1980; Sekimoto & Leibler 1993; Mortazavi & Tryggvason 2000; Hodges, Jensen & Rallison 2004; Shin & Sung 2011; Villone & Maffettone 2019; Rezghi, Li & Zhang 2022; Takeishi *et al.* 2025). The migration of deformable particles away from the wall, sometimes called the axial accumulation, is understood to be caused by nonlinear effects between particle deformation and flow field due to the presence of the wall (Leal 1980; Takemura, Magnaudet & Dimitrakopoulos 2009; Sugiyama & Takemura 2010). Along with the wall effect, the curvature or shear gradient of the velocity profile also produces a tendency for migration towards the centreline, where the shear is lower. Kaoui *et al.* (2008) demonstrated by a two-dimensional (2-D) numerical simulation in the low- Re limit that a vesicle in unbounded Poiseuille flow migrates towards the centre of the flow, as a result of asymmetric deformation between higher and lower shear sides. In the Stokes flow limit, Villone *et al.* (2016) and Villone (2019) showed by numerical analyses that a neo-Hookean elastic particle always migrates towards the channel centreline both in circular and square channel flows. They also found that the migration velocity is larger for particles that are more deformable and located closer to the channel wall, due to larger deformation.

In recent years, inertial migration of particles in rectangular channel flows at finite Re has been intensively studied in the field of microfluidics, as it is associated with a promising technology for the passive manipulation, focusing and sorting of biological cells and particles (Di Carlo 2009; Martel & Toner 2014; Stoecklein & Di Carlo 2019; Kalyan *et al.* 2021; Lee, Kim & Yang 2023; Zhang *et al.* 2024). Currently, most microfluidic devices for the separation and sorting of biological cells are designed to work mainly based on the difference in cell size. However, the operation based on their deformability is useful and of practical importance for improving diagnostic, therapeutic, biological and other performance, since many target cells, such as circulating tumour cells and malaria-infected cells, have a different stiffness from surrounding cells, and various diseases, such as cancer, blood diseases and inflammation, often accompany cell deformability alterations (Hou *et al.* 2010; Hur *et al.* 2011; McFaul, Lin & Ma 2012; Yang *et al.* 2012; Preira *et al.* 2013; Wang *et al.* 2013; Holmes *et al.* 2014; Park *et al.* 2016; Krüger *et al.* 2014a; Guo *et al.* 2017; Connolly, McGourty & Newport 2021; Stathouloupoulos *et al.* 2024). Despite the importance of the deformability of suspended particles, the fundamentals of its effect on inertial migration have not been fully understood.

The present study aims to investigate the impact of the deformability of suspended particles on their inertial migration experimentally and numerically from fluid-dynamical points of view. To simplify the problem, we treat the flow of dilute suspensions of deformable particles (hydrogel microspheres in the experiment and viscous hyperelastic particles in the numerical simulation) in a Newtonian fluid flowing through straight square channels.

Inertial migration of particles suspended in channel flows was first observed more than 60 years ago by Segré & Silberberg (1961). They reported that neutrally buoyant spherical particles in circular tube flows migrate laterally towards an annulus with a radius 0.6 times the tube at relatively low Re (Segré & Silberberg 1961, 1962). This phenomenon is referred to as the Segre–Silberberg (SS) effect and the particle focusing annulus is called the SS annulus. On the other hand, in rectangular channel flows, which are commonly used in microfluidics, suspended particles were found to first focus on a ring, called pseudo-SS ring (pSS ring), and then migrate towards several discrete points in downstream cross-sections (Chun & Ladd 2006; Choi, Seo & Lee 2011; Nakagawa *et al.* 2015; Shichi *et al.* 2017). In particular, spherical particles in square channel flows eventually focus on four points located near the centre of the channel faces at relatively low Re (Di Carlo *et al.* 2007, 2009; Zhou & Papautsky 2013; Abbas *et al.* 2014; Miura, Itano & Sugihara-Seki 2014). This focusing position is called the channel face equilibrium position or midline equilibrium position (MEP). If the focusing positions and cross-stream migration velocities can be controlled by the size, shape and deformability of suspended particles, the SS effect can be used for continuous particle separation and sorting in a label-free, external field-free manner using microchannels of simple geometry. To this end, extensive studies have been performed to develop microfluidic devices applying the SS effect to suspension flows of living cells and particles (see the review articles such as those by Di Carlo 2009; Bhagat *et al.* 2010; Karimi, Yazdi & Ardekani 2013; Stoecklein & Di Carlo 2019; Razavi Bazaz *et al.* 2020; Tang *et al.* 2020; Kalyan *et al.* 2021; Lee *et al.* 2023; Zhang *et al.* 2024, and the references therein).

The inertial focusing of spherical particles on the midlines (MEP) can be explained by the inertial lift exerted on them in square channel flows. The inertial lift is known to consist mainly of the shear gradient-induced lift, acting in the direction towards higher shear, and the wall effect, acting in the direction away from the channel wall (Ho & Leal 1974; Schonberg & Hinch 1989; Asmolov 1999; Matas, Morris & Guazzelli 2004). In circular tube flows, the balance between the outward lift due to the shear gradient and the inward lift due to the wall effect determines the radius of the SS annulus (Matas, Morris & Guazzelli 2009). In the pressure-driven flow through a square channel, on the other hand, the shear rate is higher closer to the channel walls with the maximum at the centre of the channel faces, and it is lower near the centre of the cross-section and the corners. Thus, the direction of the inertial lift due to the shear gradient is mostly outwards in the radial direction and towards the midlines, or away from the diagonal, in the azimuthal direction. The radial component, which is more pronounced than the azimuthal component, has a tendency to balance with the wall effect, so that particles approach the pSS ring first, and then migrate towards the y - or z -axis (MEP) due to the presence of the azimuthal component of the shear gradient-induced lift towards these axes.

In addition to these inertial lifts, deformable particles in channel flows experience lifts due to particle deformation (deformation-induced lift) as already noted. Thus, the inertial focusing of deformable particles is expected to be different from that of rigid particles. In fact, polyethylene glycol and alginate hydrogel particles suspended in a rectangular channel flow were demonstrated to focus closer to the channel centreline as they become more deformable (Ding *et al.* 2025). Recent numerical studies have reported several features of inertial migration specific to deformable particles in square channel flows. Schaaf & Stark (2017) showed that most of the elastic capsules migrate towards equilibrium positions on the diagonal of the channel cross-section and their focusing positions become closer to the centre for more deformable particles. The focusing position on the diagonal is referred to here as the diagonal equilibrium position (DEP) and that on the channel centre as the centre equilibrium position (CEP). Raffee, Dabiri & Ardekani

(2017) demonstrated that deformable capsules focus on the DEP in a relatively wide range of Re , in contrast to rigid particles, which focus on the MEP in the same Re range. Using hyperelastic particles, Esposito *et al.* (2022) have recently reported the existence of another equilibrium position, which is located at an intermediate position between the MEP and DEP. In certain ranges of parameters, this intermediate equilibrium position (IEP) is stable whereas both MEP and DEP are unstable.

All these numerical studies agree that equilibrium positions of deformable particles can exist on the diagonal in square channel flows at certain parameter values, but to the authors' knowledge, no experimental evidence for the presence of the DEP has been provided, except for our recent study on human red blood cells (RBCs) (Tanaka & Sugihara-Seki 2022). Human RBCs have a biconcave discoid shape at rest, with a diameter, thickness and volume of approximately 8, 2–3 μm and 94 $\mu\text{m}^3 (= V)$, respectively (Hochmuth 1987). Their equivalent diameter is $d = 2\sqrt[3]{3V/4\pi} \sim 5.6 \mu\text{m}$. RBCs are surrounded by a thin membrane, inside which is a haemoglobin solution. Due to this structure and the excess surface area relative to the volume, they are highly deformable. Tanaka & Sugihara-Seki (2022) demonstrated that at low Re with negligible inertia, RBCs migrate towards the channel centre (CEP) in square channel flows, in accord with previous studies (Goldsmith 1971; Mchedlishvili & Maeda 2001; Sasaki *et al.* 2017; Losserand, Couplier & Podgorski 2019). In contrast, at finite Re , they focus near four points on the diagonals, indicating the presence of the DEP. Since RBCs have a rather specific shape, biconcave discoid, our first aim of the present study is to demonstrate experimentally the presence of the DEP using initially spherical deformable particles. To this end, using hydrogel spheres with 5.2 μm diameter and square channels with 50 μm width, we experimentally investigate their inertial focusing in square channel flows. The obtained particle distributions in the channel cross-section are compared with those of RBCs or rigid spherical particles with similar sizes to explore the effect of particle deformation on their migration in square channel flows.

These hydrogel particles with a diameter of 5.2 μm are the largest of their kind that can currently be synthesised and the square channels used in this study, 50 μm wide (600 mm long), are the smallest commercially available. Thus, it is difficult to perform further experiments with different parameters, since suspended particles need to have a finite size ($\gtrsim 0.07$) relative to the channel width for inertial focusing (Di Carlo *et al.* 2007; Bhagat *et al.* 2008). Instead, we conduct numerical simulations for a viscous hyperelastic particle suspended in square channel flows, using a full Eulerian method (Sugiyama *et al.* 2011). By comparing the numerical and experimental results, we estimate the stiffness of the hydrogel particles and compare the obtained value with reported Young's moduli for similar particles. Next, the impact of the deformability of the particles on their inertial focusing is investigated numerically by systematically changing the Reynolds number Re and the capillary number Ca (or the Laplace number, La , defined as the ratio of the particle Reynolds number and the capillary number; see § 2.1). Several types of focusing patterns of the particles in the cross-section are obtained. As the particles become more deformable, the focusing pattern shifts from four-point focusing on the MEP, to eight-point focusing on the MEP and DEP, to four-point focusing on the DEP, and to single-point focusing on the CEP. These transitions of the particle focusing pattern are discussed in terms of the interplay between the inertial lift and the particle deformation-induced lift. In contrast to a previous numerical study (Esposito *et al.* 2022), we observe a bistable state of the MEP and DEP, but no single focusing on the IEP.

The present numerical computations indicate that the stability of the channel centre (CEP) is changed at $La \sim 8$ for the blockage ratio of 0.2; it is stable for $La < 8$ and unstable for $La > 8$. This numerical result is accounted for by the lateral force exerted

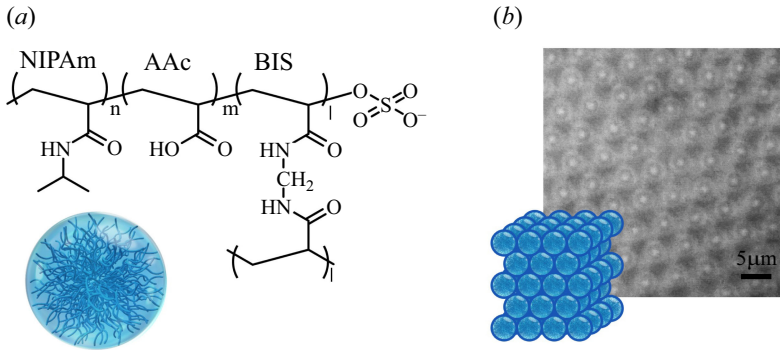


Figure 1. (a) Chemical structure of hydrogel microspheres and (b) optical microscopy image of packed hydrogel microspheres (diameter $d = 5.2 \mu\text{m}$). NIPAm, *N*-isopropylacrylamide; BIS, *N,N'*-methylenebis(acrylamide); AAc, acrylic acid.

on the hyperelastic particle near the channel centre under the assumption of small Re and Ca . The discussion is based on the asymptotic expansion of the lateral force in terms of Re and Ca , together with the numerical results for rigid spheres at $Ca = 0$ and for hyperelastic particles at $Re = 0$.

In this manuscript, the experimental and numerical methods are described in § 2. The experimental results using hydrogel particles are shown in § 3.1. The numerical results, including the comparison with the experimental results and discussion, are presented in § 3.2. Section 3.3 is devoted to the discussion of the stability of the CEP based on the inertial lift and deformation-induced lift. Concluding remarks are drawn in § 4. In Appendix A, the details of the numerical method for a rigid sphere using the immersed boundary method are described.

2. Methods

2.1. Dimensionless parameters

If suspended particles are neutrally buoyant rigid spherical particles with diameter d and the suspending fluid is a Newtonian fluid with density ρ and viscosity μ , then important dimensionless parameters for the inertial migration in square channel flows are the Reynolds number $Re = \rho U D / \mu$ and the blockage ratio $\kappa = d / D$, where D and U represent the channel width and the average flow velocity, respectively. The particle Reynolds number is defined as $Re_p = Re \cdot \kappa^2$. We consider here the case in which the concentration of particles is low enough that particle–particle interactions can be neglected. In the case of elastic particles with elastic modulus G , the capillary number $Ca = \mu U / DG$, qualifying the ratio between the viscous stress and the elastic stress, is added as a control parameter, and d represents the undeformed diameter of the particles. The ratio between Re_p and Ca gives the Laplace number $La = Re_p / Ca = \rho d^2 G / \mu^2$, which is expressed in terms of the fluid and particle properties, independent of the flow velocity and channel width.

2.2. Materials and experimental methods

As deformable suspended particles, we used poly(*N*-isopropylacrylamide)-based hydrogel microspheres fluorescently labelled by 5-aminofluorescein (figure 1) (Kawamoto *et al.* 2023, 2024). These hydrogel particles were synthesised by a modified aqueous precipitation polymerisation method under the condition of *N*-isopropylacrylamide

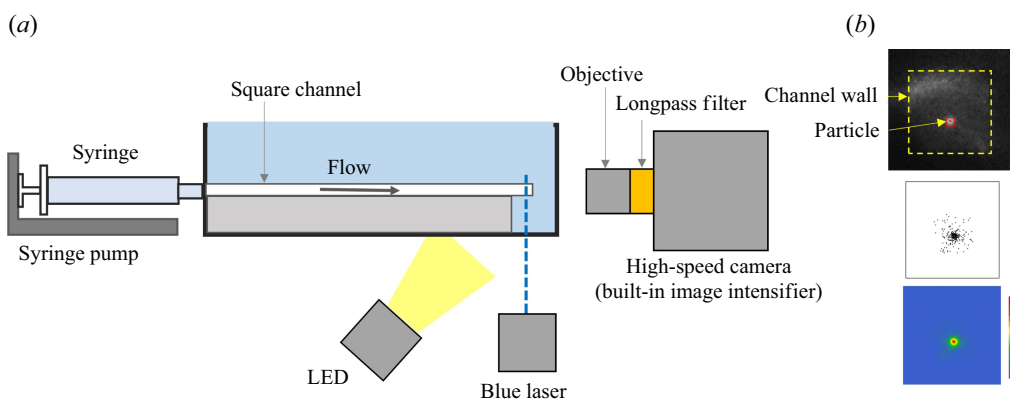


Figure 2. (a) Experimental set-up and (b) method of image analyses: an example of obtained images (top), distribution of particle centroids (middle) and probability density function (p.d.f.) in the channel cross-section (bottom).

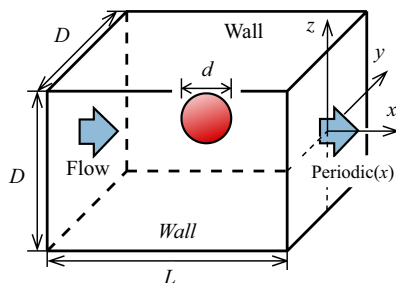


Figure 3. Configuration for the numerical simulation ($L = 2D$).

(NIPAm) 70 mol %, N, N' -methylenebis (acrylamide) (BIS) 1 mol % and acrylic acid (AAc) 29 mol %. As shown in figure 1(b), the particle size is almost uniform, with an average diameter $d = 5.2 \mu\text{m}$. Details of these hydrogel microspheres and their deformation at the air/water interface are described by Minato *et al.* (2018).

The hydrogel particles were suspended in glycerol aqueous solution at volume fractions of 0.003–0.01 %. The density and viscosity of the solution are $1.05 \times 10^3 \text{ kg m}^{-3}$ and 1.72 mPa s, respectively, at 22 °C. As shown in figure 2(a), a syringe pump (Nexus 6000, ISIS) was used to infuse the suspension into a straight glass tube with a square cross-section of width $D = 50 \mu\text{m}$ and length $L = 50\text{--}600 \text{ mm}$ (VetroCom). Face-on fluorescence images of the tube cross-section near the outlet (1–2 mm upstream of the outlet) were taken along the tube axis from the downstream side using a high-speed camera with a built-in image intensifier (SV200i, Photron) under the illumination of a 3 W blue laser (Kentech), equipped with a longpass filter (SCHOTT OG-530, Edmund Optics) and an ultralong working distance objective (SLMPLN 50 \times , 100 \times , Olympus). An LED light was also used to detect the tube wall. When using a 50 \times objective, the pixel size is $0.268 \times 0.268 \mu\text{m}^2$. The images obtained were analysed using the public domain software ImageJ (NIH) to detect the position of the centroid of each particle in the cross-section. In each experiment, we counted more than 300 particles to determine their distribution and the probability densities (figure 2b).

2.3. Numerical methods

In our numerical simulations, we considered a single deformable particle flowing in a channel of length L with a square cross-section with side D as shown in figure 3. The channel is filled with a Newtonian fluid and the pressure-driven Poiseuille flow is directed along the x -coordinate. We assume that both the fluid and the particle are incompressible and have the same density ρ and dynamic viscosity μ , which means the particle is neutrally buoyant. The deformable hydrogel particle is modelled as a viscous hyperelastic solid rather than a capsule or a fluid drop. We specifically employ the neo-Hookean model (Mooney 1940; Rivlin 1948; van Hoogstraten, Slaats & Baaijens 1994), which has the simplest constitutive law for such hyperelastic materials. The particle is initially spherical with a diameter d under unstressed conditions.

This study explores a broad parameter space to achieve more comprehensive understandings rather than to reproduce specific phenomena. We employed two dimensionless numbers Re and Ca as the governing parameters.

Our simulation employs the fully Eulerian method developed by Sugiyama *et al.* (2011). This method is a finite difference method based on the VOF method by Hirt & Nichols (1981), solving the fluid–structure coupling problem using the VOF function. To derive the nondimensional governing equations, we introduce the following non-dimensional variables,

$$\frac{\partial}{\partial t} = \frac{U}{D} \frac{\partial}{\partial t^*}, \quad \mathbf{u} = U \mathbf{u}^*, \quad p = \rho U^2 p^*, \quad \nabla = \frac{1}{D} \nabla^*. \quad (2.1)$$

Then, we obtain the non-dimensional governing equations:

$$\nabla^* \cdot \mathbf{u}^* = 0, \quad (2.2)$$

$$\frac{\partial \mathbf{u}^*}{\partial t^*} + (\mathbf{u}^* - \mathbf{e}_x V_x^*) \cdot \nabla \mathbf{u}^* = -\nabla^* p^* + \frac{1}{Re} \nabla^{*2} \mathbf{u}^* + \frac{1}{Re Ca} \nabla^* \cdot (\alpha \mathbf{B}^*) - \mathbf{e}_x \frac{dP^*}{dx^*}_{drive}, \quad (2.3)$$

$$\frac{\partial \alpha}{\partial t^*} + (\mathbf{u}^* - \mathbf{e}_x V_x^*) \cdot \nabla \alpha = 0, \quad (2.4)$$

$$\frac{\partial \mathbf{B}^*}{\partial t^*} + (\mathbf{u}^* - \mathbf{e}_x V_x^*) \cdot \nabla \mathbf{B}^* = \mathbf{L}^* \cdot \mathbf{B}^* + \mathbf{B}^* \cdot \mathbf{L}^{*\top}, \quad (2.5)$$

where V_x denotes the x -component of the particle's velocity, α denotes the volume fraction of solid, $\mathbf{L} = \partial \mathbf{u} / \partial \mathbf{x}$ denotes the velocity gradient tensor and $\mathbf{B} = \mathbf{F} \cdot \mathbf{F}^\top$ denotes the left Cauchy–Green deformation tensor, where $\mathbf{F} = \partial \mathbf{x} / \partial \mathbf{X}$ is the deformation gradient, \mathbf{x} is the current coordinates and \mathbf{X} is the reference coordinates (Bonet & Wood 2008).

Following Sugiyama *et al.* (2011), we monolithically describe the pressure over the entire incompressible media. Further, we write the mixture stress as $\boldsymbol{\sigma} = -p\mathbf{I} + (1 - \alpha)\boldsymbol{\sigma}'_f + \alpha\boldsymbol{\sigma}'_s$, where $\boldsymbol{\sigma}'$ denotes the deviatoric stress, and the subscript f and s refer to the fluid and solid phases, respectively. The deviatoric tensor is defined as $\mathbf{T}' = \mathbf{T} - \text{tr}(\mathbf{T})\mathbf{I}/3$. The term dP^*/dx^*_{drive} indicates the constant driving pressure, which is analytically derived from the solution of duct flow without particles (Cornish 1928):

$$-\frac{dP^*}{dx^*_{drive}} = \frac{4}{KRe}, \quad K \approx 0.160577 \dots \quad (2.6)$$

Although the fully Eulerian method (Sugiyama *et al.* 2011) has been demonstrated to facilitate solving various problems such as flows bounded by compliant walls (Rosti & Brandt 2017; Esteghamatian, Katz & Zaki 2022) and flows including soft particles (Rosti & Brandt 2018; Rosti *et al.* 2018; Prasad, Sharma & Kulkarni 2022), the numerical solution is

likely to be unstable especially when long-time computation is required, as in the present study. Such a numerical instability is more pronounced with the higher advection speed of the fluid–structure interface.

In this study, we investigate the motion of particles moving downstream in the x -direction. The particle's x -coordinate can be fixed within the computational domain, as the computational system is homogeneous in the x -direction. This technique is implied by the term including $e_x V_x^*$ in (2.3)–(2.5), minimising the advection velocity. Note that this formulation is based on a coordinate transformation, in which the x coordinate in the computational space attaches to the particle centroid, and holds even if V_x^* varies with time. For the time and spatial discretisation of the advection terms with the constant velocity $(\partial_t^* - e_x V_x^* \cdot \nabla)$ in (2.3)–(2.5), a discrete Fourier interpolation (Gerz, Schumann & Elghobashi 1989) is applied to reduce numerical diffusion and instability.

Furthermore, the MTHINC scheme (Ii *et al.* 2012b) is employed for the convection of the volume fraction $(\partial_t^* \alpha + (\mathbf{u}^* \cdot \nabla) \alpha)$ in (2.4). The MTHINC scheme approximates the VOF function distribution across the elastic-fluid interface using a hyperbolic tangent function, effectively suppressing interface smearing and numerical instability. The sharpness parameter relative to the grid is set to $\beta = 2$, following the rigid particle simulation in Appendix A.

Other spatial derivative terms are discretised using the second-order central scheme except for the advection term of \mathbf{B} . The advection term $\mathbf{u}^* \cdot \nabla \mathbf{B}^*$ in (2.5) is spatially discretised by the fifth-order WENO scheme (Liu, Osher & Chan 1994; Jiang & Shu 1996).

For the time procedures, the second-order Adams–Bashforth scheme (Canuto *et al.* 2012) is applied to the convection term of $\mathbf{u}^* \cdot \nabla \mathbf{u}^*$ in (2.3), $\mathbf{u}^* \cdot \nabla \mathbf{B}^*$ and the right-hand side of (2.5). The Crank–Nicolson scheme (Canuto *et al.* 2012) is applied to the viscous and elastic terms in (2.3). To implicitly treat the pressure together with (2.2), the Simplified Marker-and-Cell (SMAC) method (Amsden & Harlow 1970) is employed. To solve the Poisson equation directly, we use a fast Fourier transform (FFT) and a tri-diagonal matrix algorithm (TDMA).

For the boundary conditions, we apply periodic conditions along the channel and no-slip conditions for the walls. The computational domain is discretised with a grid size of $256 \times 128 \times 128$ and $128 \times 64 \times 64$ for $\kappa = 0.1$ and $\kappa = 0.2$, respectively. The channel length and width are defined as $L = 2$ and $D = 1$, respectively, and the grid resolution is given by $\Delta x = \Delta y = \Delta z = 1/128$ or $1/64$. The effect of channel length L associated with the periodic boundary condition is discussed and the present choice of $L/D = 2$ is validated in figure S1 of the Supplementary material, which is available at <https://doi.org/10.1017/jfm.2025.10574>.

The Courant–Friedrichs–Lewy (CFL) number is fixed at a constant value of 0.0625, and the time step Δt is determined based on the maximum propagation velocity U_{prop} . Here, U_{prop} is determined by comparing the maximum advection velocity $U_{adv} = \max(|u_x - V_x|, |u_y|, |u_z|)$ and the shear/transverse wave speed in the elastic particle $U_{els} = \sqrt{G/\rho}$.

$$U_{prop} = \max(U_{adv}, U_{els}), \quad (2.7)$$

$$\Delta t = \frac{\text{CFL} \cdot \Delta x}{U_{prop}}. \quad (2.8)$$

In particular, for the advection terms, we employ the advective interpolation scheme (Kajishima & Taira 2016, § 3.5.1), which satisfies the relations $\partial_j(u_j u_i) = u_i \partial_j u_j + u_j \partial_j u_i$ in a discretised form and ensures that the momentum and the quadratic quantity are highly conserved.

We also employ the immersed boundary method (Kajishima *et al.* 2001) for a calculation of a rigid particle, as detailed in [Appendix A](#), and compare the results with those of the deformable particles.

2.4. Taylor deformation parameter

The Taylor deformation parameter \mathcal{T} is introduced as a measure of the deformation of elastic particles. This parameter is mathematically defined by the lengths of the semi-major axes l_m and semi-minor axes l_n of an ellipse in a two-dimensional plane (Taylor 1934),

$$\mathcal{T} = \frac{l_m - l_n}{l_m + l_n}. \quad (2.9)$$

Here, \mathcal{T} decreases as the shape of an object approaches a circle, whereas greater deformations result in higher \mathcal{T} values. As this study involves three-dimensional particles, it is necessary to determine quantities corresponding to the semi-major and semi-minor axes in a spherical geometry. In this study, we evaluate \mathcal{T} using another well-known approach by approximating the shape of a deformed sphere as a triaxial ellipsoid with the same moment of inertia to capture the deformation in three dimensions (Ramanujan & Pozrikidis 1998; Takeishi *et al.* 2019). The principal moments of inertia $I_{a,b,c}$ relative to the centre of mass of the triaxial ellipsoid can be determined using the VOF function α . The semi-axes of the triaxial ellipsoid a, b, c are obtained from the following equations:

$$a = \sqrt{\frac{5}{2M}(-I_a + I_b + I_c)}, \quad b = \sqrt{\frac{5}{2M}(I_a - I_b + I_c)}, \quad c = \sqrt{\frac{5}{2M}(I_a + I_b - I_c)}. \quad (2.10)$$

where M denotes the mass of the particle. Finally, l_m and l_n are determined as $l_m = \max(a, b, c)$, $l_n = \min(a, b, c)$.

3. Results and discussion

3.1. Experimental results

[Figures 4\(a\)–4\(e\)](#) show representative distributions of hydrogel particles in the channel cross-section for $L/D = 1000–12\,000$ at $Re = 0.1–10$, and [figure 4\(f\)](#) shows probability density functions (p.d.f.s) of particles for $L/D = 12\,000$. At $Re = 0.1$ shown in [figure 4\(a\)](#), particles gradually approach the centre of the channel cross-section, and focus near the centre at the most downstream (see [figure 4f](#)). This axial accumulation is consistent with previous studies for deformable particles at low Re (Karnis *et al.* 1963; Goldsmith 1971). At $Re = 0.5$ and 1, particles migrate inwards until they focus along a small ring together with the channel centre. At $Re = 5$ and 10, particles are aligned along a ring (pSS ring) upstream and focus near four points on the diagonals downstream. This focusing position corresponds to the DEP. It is noteworthy that the particle focusing positions move away from the channel centre with increasing Re .

For the particle distributions shown in [figures 4\(a\)–4\(e\)](#), [figures 5\(a\)](#) and [5\(b\)](#) plot the average distance of the particle centroid from the channel centre, $\langle r \rangle / (D/2)$, and the number fraction of particles located within $\pm 10^\circ$ from the diagonals, P_d (see the inset of [figure 5b](#)), as a function of L/D . The error bar represents the standard deviation (only the upper or lower side is plotted). At low Re (≤ 1), the average distances first decrease with L/D up to 6000 and become almost constant further downstream, while P_d keeps nearly constant values $\sim 20^\circ/90^\circ = 0.22$, that is, for random distribution, for all L/D . This result indicates that, at $Re \leq 1$, particles have reached equilibrium positions in the radial direction within a distance of $L/D = 6000$ from the channel inlet, with no preferential

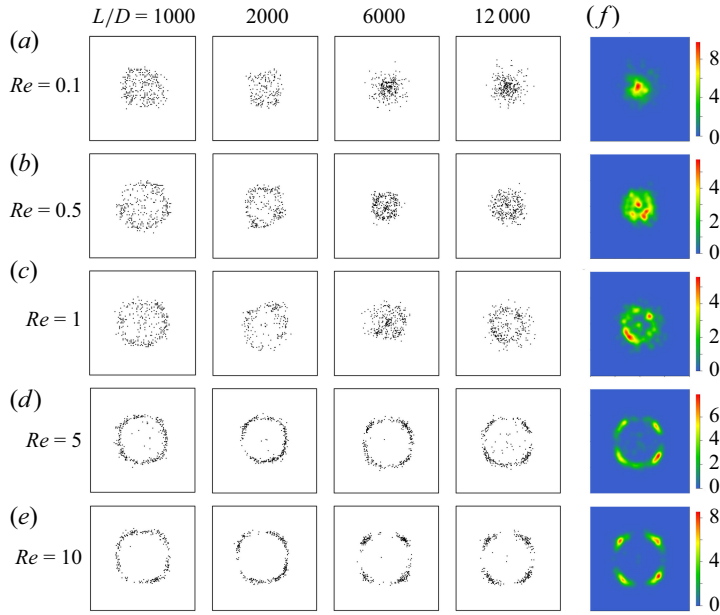


Figure 4. (a)–(e) Distributions of hydrogel particles ($d = 5.2\text{ }\mu\text{m}$, $D = 50\text{ }\mu\text{m}$) and (f) probability density functions (p.d.f.s) at $L/D = 12\,000$ ($L = 600\text{ mm}$).

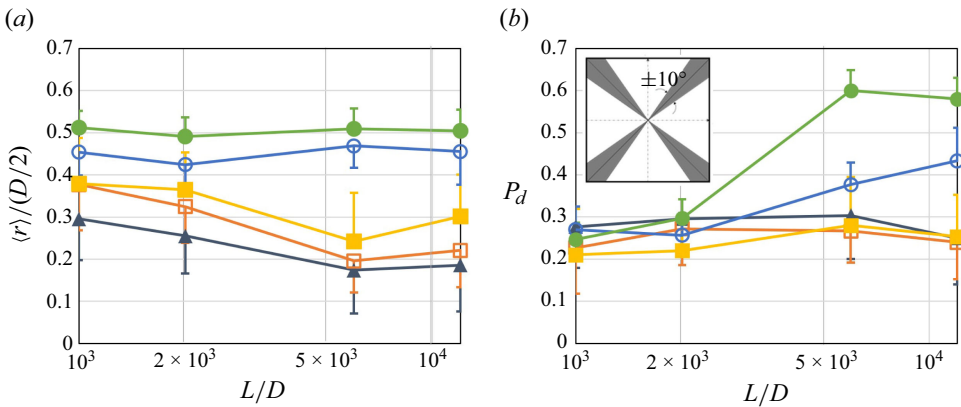


Figure 5. (a) Average distances $\langle r \rangle / (D/2)$ of hydrogel particles from the channel centre and (b) number fraction P_d of particles located within $\pm 10^\circ$ from the diagonals, at $Re = 0.1$ (triangles), 0.5 (open squares), 1 (closed squares), 5 (open circles) and 10 (closed circles).

distribution in the azimuthal direction. In contrast, the average distances at $Re \geq 5$ remain nearly constant independent of L/D (≥ 1000) and P_d increases almost monotonically with L/D . This result implies that, at $Re \geq 5$, particles have reached an equilibrium radial position (pSS ring) in a short distance from the channel inlet ($L/D < 1000$) and migrate circumferentially towards the diagonal further downstream. The first part of this migration, mostly in the radial direction towards the pSS ring, is known as the first phase of the inertial migration, which represents a rather rapid motion, and the following slow migration along the pSS ring towards the DEP is the second phase. The present result demonstrates that hydrogel particles also exhibit a two-phase property of the inertial migration in square channel flows.

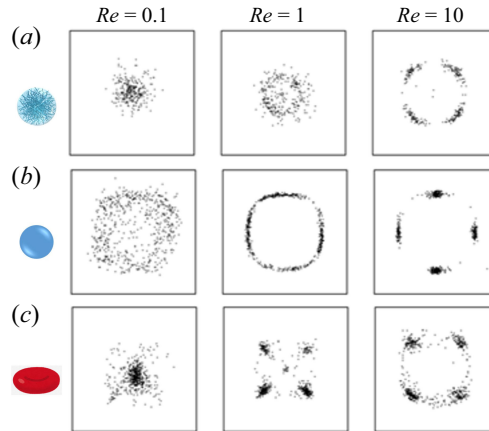


Figure 6. Distributions of (a) hydrogel particles in glycerol aqueous solutions, (b) rigid spherical particles ($d = 5 \mu\text{m}$) in glycerol aqueous solutions and (c) human red blood cells in blood plasma (Tanaka & Sugihara-Seki 2022) ($D = 50 \mu\text{m}$, $L = 600 \mu\text{m}$).

Figure 6 illustrates a comparison of the distribution of hydrogel particles with those of rigid spherical particles ($d = 5 \mu\text{m}$) and human red blood cells (RBCs) reported in our previous study (Tanaka & Sugihara-Seki 2022). RBCs have a biconcave discoid shape at rest, with an equivalent diameter $d \sim 5.6 \mu\text{m}$, and they are highly deformable, as noted in § 1. In the case of small inertia ($Re = 0.1$), deformable particles (hydrogel particles and RBCs) focus near the channel centre, whereas rigid spherical particles are dispersed widely in the channel cross-section, as inferred from the motion of rigid spherical particles along the channel axis in the Stokes flow. On the other hand, in the case of finite inertia at $Re = 10$, both hydrogel particles and RBCs focus near the DEP, whereas rigid spherical particles focus near the MEP. This result indicates that the focusing on the DEP results from the effect of particle deformation. At $Re = 1$, rigid particles focus along the pSS ring with higher concentrations near the MEP. With regards to deformable particles, hydrogel particles are aligned along a small ring together with the channel centre, whereas RBCs focus on four points on the diagonals together with the centre. Although these two focusing patterns of deformable particles may appear different, they are essentially similar and the difference presumably arises from differences in the size of the pSS ring. Possibly due to differences in the deformability and shape of the suspended particles and/or the rheological properties of the suspending media, the pSS ring for the hydrogel particles is much smaller than that for RBCs. Since the flow field near the channel centre is nearly axisymmetric, the azimuthal component of the lift exerted on the hydrogel particles on the pSS ring is much weaker than that on the RBCs. As a result, the focusing in the second phase of the inertial migration is much slower for the hydrogel particles than that for RBCs.

3.2. Numerical results

The elastic modulus G or the Laplace number La for hyperelastic particles was searched for the one that best reproduces the distribution of hydrogel particles experimentally observed, since the elastic moduli of these particles are unknown. First, numerical simulations with $\kappa = 0.1$ and $Re = 10$ corresponding to figure 4(e) were performed for various La values. With La set to 5, 10 and 50, trajectories of the centroid of hyperelastic particles projected onto the channel cross-section are shown in the upper panels of figure 7(a–c), starting from various initial positions (open circles) located in the lower right half of the first quadrant to final positions (closed circles) during a dimensionless

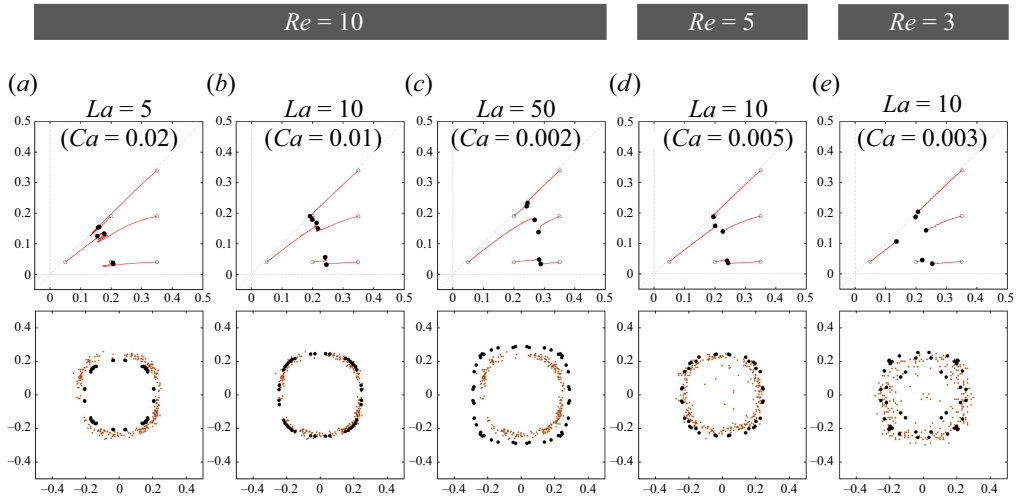


Figure 7. Comparisons between the experimental and numerical results for the particle distribution in the channel cross-section at corresponding distances from the inlet ($\kappa = 0.1$). The upper panels: trajectories of the centroid of hyperelastic particles from initial positions (open circles) to final positions (closed circles) during the dimensionless time (a)–(c) $t^* (\equiv tU/D) \sim 2000$ and (d,e) 1000, in the first quadrant of the cross-section. The lower panels: final positions in the entire cross-section (dots) and corresponding particle distributions obtained experimentally at (a)–(c) $L/D = 2000$, (d,e) 1000.

time $t^* (\equiv tU/D) \sim 2000$. The lower panels illustrate their final positions in the entire cross-section, obtained by taking into account the symmetry with respect to the y -, z -axes (midlines) and diagonals, along with the distribution of hydrogel particles observed experimentally at $L/D = 2000$ (figure 4e). Comparisons between experimental and numerical results in figure 7(a–c) indicate that the experimentally obtained distribution is best reproduced when adopting $La = 10$. To confirm this value, the numerical simulations with $La = 10$ for different Re and different distances L/D are performed and compared with corresponding distributions of hydrogel particles. Figures 7(d) and 7(e) are two examples, in which the experimental and numerical results are in good agreement in favour of $La \sim 10$.

The Laplace number $La = 10$ gives the elastic modulus $G = 1.04$ kPa, using the values for the density and viscosity of the fluid and the particle diameter. Assuming a Poisson's ratio of 0.5, Young's modulus of the hydrogel particles is estimated to be ~ 3.13 kPa. Banquy *et al.* (2009) used atomic force microscopy to measure Young's modulus of similar but much smaller hydrogel particles and reported that it ranges from 18 kPa for particles with a cross-linker content of 1.7 mol % to 211 kPa for particles with a cross-linker content of 15 mol %. The present estimate of Young's modulus ~ 3.1 kPa for particles with a cross-linker content of 1 mol % is slightly smaller but comparable to extrapolations from these reported values. Although the distributions of hydrogel particles experimentally obtained at $Re \geq 3$ are successfully reproduced by the present numerical simulation, comparisons at lower $Re (\lesssim 1)$ are difficult because of the large computational time required for small particles with $\kappa = 0.1$ to reach specific focusing positions at lower Re .

To explore the effect of particle deformation on the inertial migration in wider ranges of Re and La , we computed the motion and deformation of hyperelastic particles with larger blockage ratios. Figure 8 shows trajectories of the particle centroid starting from two initial positions $(y_0^*, z_0^*) = (0.35, 0.07)$ and $(0.35, 0.28)$, their final positions in the entire cross-section obtained from symmetry considerations and final particle shapes, for $\kappa = 0.2$ at

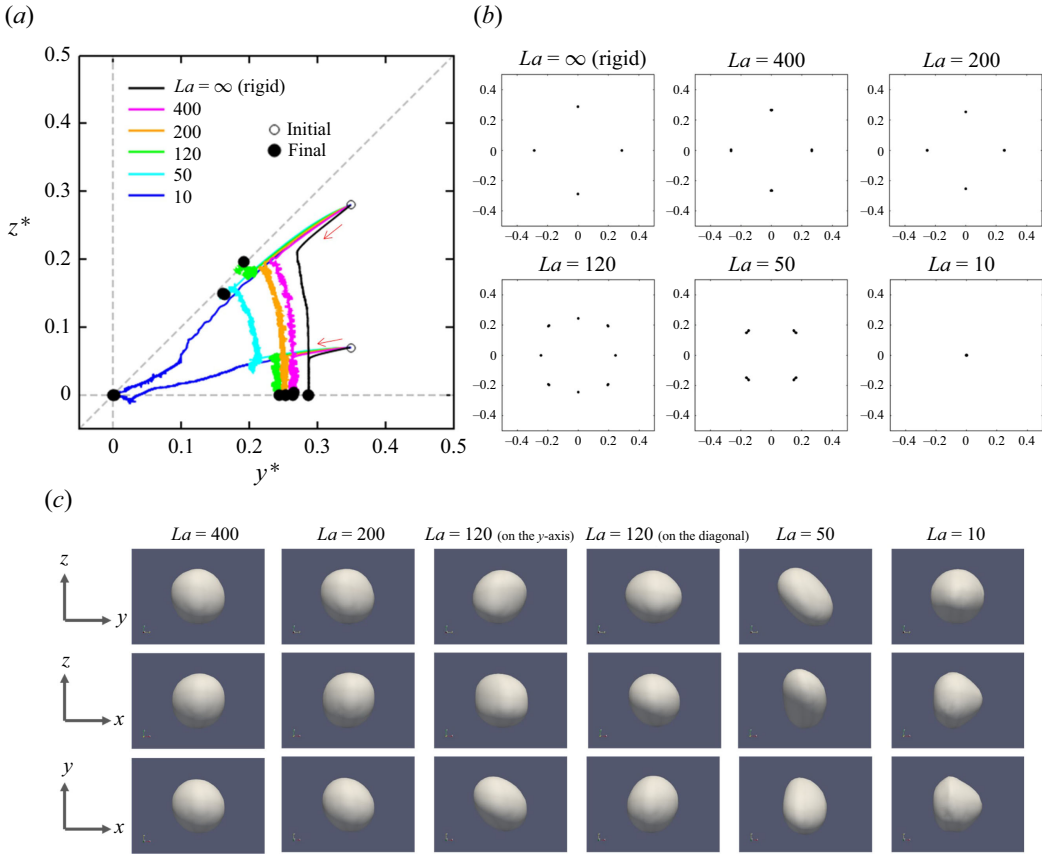


Figure 8. (a) Trajectories of the centroid of hyperelastic particles in the first quadrant of the channel cross-section, (b) the final positions in the entire cross-section and (c) snapshots of particles at the final position, for $\kappa = 0.2$ at $Re = 40$.

$Re = 40$ in the range of La from 10 to ∞ (rigid spherical particles). The computations for rigid spherical particles were conducted using a computer scheme reported previously (Nakagawa *et al.* 2015). In all cases, particles first migrate inwards until they reach a certain distance from the channel centre and then move circumferentially towards the y -axis or diagonal, except in the case of $La = 10$, where they continue to move towards the channel centre. This feature clearly shows the two-phase property of the inertial migration in square channel flows, and the circumferential motion in the second phase is performed along the pSS ring towards a stable equilibrium position. The final position of rigid spherical particles is located on the y -axis (MEP), in agreement with previous studies (Di Carlo *et al.* 2009; Miura *et al.* 2014). The hyperelastic particles with relatively large La ($= 400$ and 200) also exhibit focusing on the MEP, and the focusing positions move closer to the channel centre with decreasing La . On the other hand, for smaller La ($= 50$), the final focusing positions are located on the diagonals (DEP). In the case of $La = 120$ between these two cases, hyperelastic particles focus on eight points on the midlines and diagonals in the entire cross-section, implying a bistable state of the MEP and DEP. At the smallest value of La ($= 10$), a stable equilibrium position is located on the channel centre even at moderate Re ($= 40$).

Figure 8(c) depicts snapshots of hyperelastic particles located at the final position, when viewed along the x -, y - and z -axes. Note that these are shapes at a certain instant in

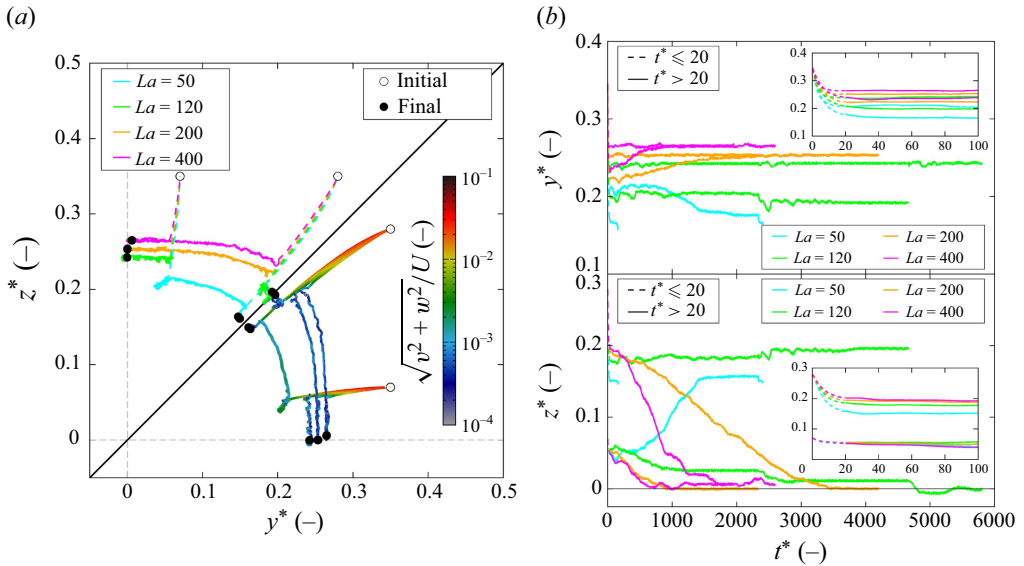


Figure 9. (a) Trajectories (above the diagonal) are shown with dashed lines for $t^* \leq 20$ and solid lines for $t^* > 20$, while the magnitude of the in-plane velocity (below the diagonal) is represented by the colour bar. (b) Time evolution of the dimensionless y^* -coordinate y^* (top) and z^* -coordinate z^* (bottom), with the inset focusing on the t^* -axis ranges from 0 to 100. The initial positions are $(y_0^*, z_0^*) = (0.35, 0.07), (0.35, 0.28)$. The blockage ratio $\kappa = 0.2$ and $Re = 40$.

time. It is seen from figure 8(c) that, in general, a smaller La results in a larger particle deformation, as expected. However, the shift of the final position towards the channel centre with decreasing La suppresses that increase (see figures 10b and 10c). Notably, for $La = 10$, the deformation is rather small and the particle has an almost axisymmetric shape, rounded at the front and nearly flat at the back, since its final position is very close to the channel centre, where the shear rate is small and axisymmetric.

To demonstrate the two-phase property of inertial migration in more detail, figure 9 shows the lateral speed and the movement of the particle centroid. The particle is seeded at the same initial positions as in figure 8 or symmetric positions relative to the diagonal for $La = 50$ –400. In the upper left half of figure 9(a), the trajectories of the particle are drawn with dashed lines for $t^* \leq 20$, corresponding to a roughly estimated dimensionless time for the first phase, and the trajectories for $t^* > 20$ are drawn with solid lines. In the lower right half of figure 9(a), the lateral velocity magnitude of the particle is indicated by colour along the trajectories. The variations of the position of the particle centroid are plotted as a function of time in figure 9(b). It is seen from figure 9(a) that the lateral velocity in the first phase is $O(10^{-2})$ relative to the mean flow velocity, whereas that in the second phase is $O(10^{-3})$ for $La = 50$ and $O(10^{-4})$ for $La = 120$ –400. The rapid migration in the first phase and the slow migration in the second phase can be also confirmed from figure 9(b) together with the insets. A distinct feature observed in figure 9(b) is that the centroid of hyperelastic particles fluctuates even after approaching a stable position.

In each case shown in figures 8 and 9, the focusing pattern of particles can be easily identified. However, for some parameter values including La between 10 and 50 at $Re = 40$, the process became highly challenging. In some cases, the migration velocity of the particle becomes very small before reaching the midline, diagonal or centre. In other cases, excessive deformation caused numerical instability. The former case suggests the presence of another type of equilibrium position, presumably located between the MEP and DEP

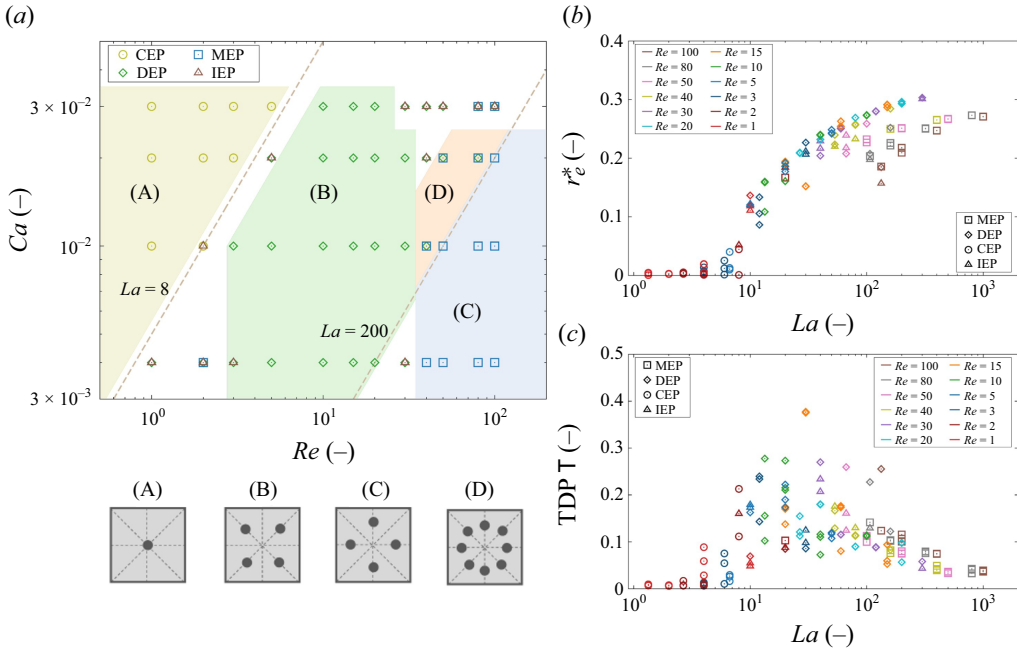


Figure 10. (a) Particle focusing patterns, (b) distance of the final position from the channel centre and (c) time average of T at the final position for $\kappa = 0.2$. Each dataset is calculated for each Re and Ca from three initial positions: $(y_0^*, z_0^*) = (0.0625, 0.03125)$, $(0.3125, 0.03125)$, $(0.3125, 0.28125)$. Each symbol represents a focusing position: circles for CEP, squares for MEP, diamonds for DEP and triangles for IEP. Each coloured region corresponds to a focusing pattern: (A) CEP, (B) DEP, (C) MEP and (D) MEP + DEP.

on the pSS ring. This focusing position may correspond to the equilibrium position called the intermediate equilibrium position (IEP) by Esposito *et al.* (2022). Their numerical analyses showed that hyperelastic particles suspended in square channel flows migrate to the IEP between the midline and the diagonal (eight equilibrium positions in the whole cross-section) in a rather wide range of parameters. In the present study, it is practically difficult to determine whether the particle's intermediate position is a focusing position or a transient one. This is mainly because the lateral migration in the second phase is generally slow as seen in figure 9, and it becomes extremely slow near the transitions between different focusing positions.

To avoid ambiguity, we performed the computation in fixed time steps of 4×10^6 at a constant CFL = 0.0625, starting from several initial positions of the particle for various Re and Ca at $\kappa = 0.2$. Each final position is classified into four types as follows: CEP when the final position is located within $0.05D$ from the channel centre, MEP or DEP when the azimuthal angle of the final position from the midline or diagonal is within $\pm\pi/30$, and IEP for the rest. When the final position is categorised as the IEP, the extra computation of 3×10^6 steps is conducted and its final position is checked again according to the above criteria. This procedure is repeated as far as the final position is categorised as the IEP, up to the total time steps of 2.2×10^7 . The computational time $t^* = tU/D$ for 2.2×10^7 time steps depends on U_{prop} (which is primarily determined by Re and Ca) under the constant CFL number, with the maximum $t^* \sim 1.029 \times 10^4$ for $Re = 50$ and $Ca = 0.02$, and the minimum $t^* \sim 1.359 \times 10^3$ for $Re = 1$ and $Ca = 0.004$.

The results of such a classification with three initial positions $(y_0^*, z_0^*) = (0.0625, 0.03125)$, $(0.3125, 0.03125)$ and $(0.3125, 0.28125)$ are shown in figure 10(a), in which

three symbols representing the type of the final positions are superimposed at each point in the parameter space for $1 \leq Re \leq 10^2$ and $4 \times 10^{-3} \leq Ca \leq 3 \times 10^{-2}$. When three symbols are identical (in most of these cases, the three final positions are very close to each other), it is highly suggested that the final position represents a stable equilibrium position or a focusing position observed in the experiment. Such cases consist of a single-point focusing at the CEP (pattern A, area coloured yellow in [figure 10a](#)), four-point focusing at the DEP (pattern B, area coloured green) and four-point focusing at the MEP (pattern C, area coloured blue). In the parameter space between patterns (B) and (C) for $Ca \geq 10^{-2}$ highlighted in orange, a bistable state of the DEP and MEP is suggested. This focusing pattern, corresponding to the pattern for $La = 120$ in [figure 8\(b\)](#), is referred to as pattern (D). In uncoloured areas near the edge of coloured areas, where transitions between different focusing patterns are expected, the IEP (triangles) is observed together with other symbols. This indicates that all three final positions do not converge to a single point in the current computational time. Although single or multiple stable states of equilibrium positions (CEP, DEP, MEP and IEP) may be reached after much longer computations, it is currently hard to identify the focusing pattern in these areas. As far as examined in the present study, we do not observe a sole focusing pattern at the IEP. This is a significant difference from the results of Esposito *et al.* (2022), as discussed later.

The effect of particle deformability is dominant and that of inertia is small in the upper left of [figure 10\(a\)](#), and *vice versa* in the lower right. From top left to bottom right, coloured areas sequentially represent patterns (A), (B) and (C). There is an area of pattern (D) between patterns (B) and (C). A notable feature in [figure 10\(a\)](#) is that the boundary between patterns (A) and (B) lies approximately on a straight line with $La = 8$, which is related to the stability of the CEP. Similarly, the stability of the DEP may be changed on another line with $La \sim 200$. The implication of the former is discussed in § 3.3. The latter is beyond the scope of the present study and will be left for future work.

We consider the transitions of the particle focusing pattern shown in [figure 10\(a\)](#), based on the effects of inertia and particle deformation. As noted in § 1, the inertial lift consists mainly of the shear gradient-induced lift, acting in the direction towards higher shear, and the wall effect, acting in the direction away from the channel wall. In the square cross-section, the direction of the shear gradient-induced lift is mostly outwards in the radial direction and towards the y - or z -axis (midlines) in the azimuthal direction. Thus, rigid particles are focused on the midlines (MEP) at finite Re and small Ca (pattern C). On the other hand, if the particle deformation-induced lift is exerted on hyperelastic particles in the direction towards lower shear, as noted already, then its direction is nearly opposite to the shear gradient-induced lift, i.e. mostly inwards and towards the diagonal in the square cross-section. As a result, more deformable particles tend to focus on the diagonal (DEP) rather than on the midline (MEP), and their focusing positions approach the channel centre (CEP), as seen in [figure 10\(a\)](#). Thus, an increase in the deformation-induced lift directed towards lower shear accounts for the transition of the focusing pattern from pattern (C) through (B) to (A) shown in [figure 10\(a\)](#).

[Figures 10\(b\)](#) and [10\(c\)](#) depict the distance of the final position from the channel centre and the average of the Taylor deformation parameter \mathcal{T} during the last 50 000 steps, respectively. [Figure 10\(b\)](#) clearly shows that, at constant Re , all of MEP, DEP and IEP approach the channel centre with decreasing La . This indicates that the final positions of more deformable particles approach closer to the channel centre. All curves for the DEP roughly collapse onto a single curve, which is similar to the feature observed for capsules (Schaaf & Stark 2017). [Figure 10\(b\)](#) shows that this is also almost true for the MEP, and that the master curve for the MEP is located below the DEP master curve. Additionally,

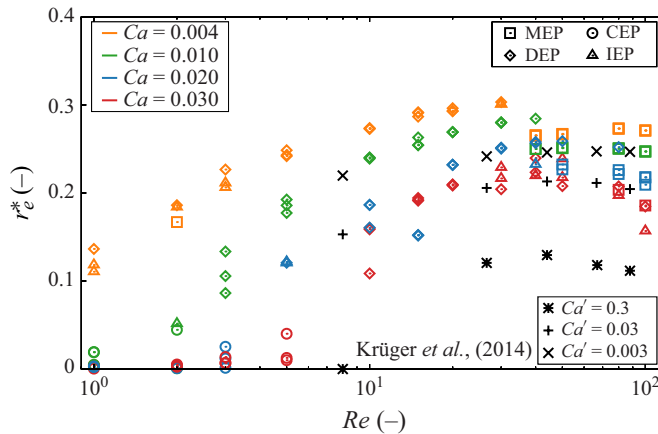


Figure 11. Distance of the final position from the channel centre. Coloured plots show results for particles in the present study, and black markers represent capsule data from Krüger *et al.* (2014b) ($\kappa = 0.2$).

the DEP appears only for $La \gtrsim 8$, below which the focusing position is changed to the channel centre (CEP), as expected from figure 10(a).

Figure 10(c) shows that \mathcal{T} at the final position increases with increasing La up to several tens, and then gradually decreases at each Re . Considering that La provides a measure of the impact of inertia relative to particle deformation, a decrease in \mathcal{T} with increasing La seems reasonable. The inverse trend for small La is explained by the fact that more deformable particles tend to approach closer to the channel centre, where smaller shear rates cause smaller deformation.

Recently, Esposito *et al.* (2022) reported focusing patterns of hyperelastic particles for $\kappa = 0.2$ in wider ranges of Re and Ca . They found four types of particle focusing patterns, among which patterns (A) and (C) are consistent with the present study. Each of patterns (A) and (C) appears in a similar range of Re and Ca in figure 10(a), whereas in their study, the focusing on the IEP emerges in the range where patterns (B) and (D) appear in the present study, and pattern (B) does not appear in the present range of $1 \leq Re \leq 10^2$ and $4 \times 10^{-3} \leq Ca \leq 3 \times 10^{-2}$. Esposito *et al.* (2022) never found pattern (D) in their whole range of parameters. These discrepancies may be due to the different models used for the particles: the particles in the present study are viscoelastic, but those in their models include no viscosity. Differences in the criteria used to categorise the focusing positions may also be possible causes of the discrepancies.

As deformable particles, capsule models have been often adopted in numerical simulations to study inertial migration. Among these studies, Krüger *et al.* (2014b) investigated the rheological properties of a capsule suspension in the pressure-driven flow between two infinite parallel plates (Misbah 2014). At a low volume fraction of particles, they demonstrated that the lateral equilibrium position of the capsules increases with increasing Re up to 45 (corresponding to ~ 60 in the present definition of Reynolds number), followed by a decrease, as shown in figure 11. Figure 11 replots the present results of the final lateral position r_e^* shown in figure 10(b) as a function of Re for various Ca , superimposing the results of Krüger *et al.* (2014b). In their study, the capillary number Ca' is defined as the ratio of a typical shear stress magnitude to a characteristic elastic particle stress κ_s/a , where κ_s and a represent the shear elasticity of the capsule membrane and the radius of the undeformed capsule, respectively. Figure 11 demonstrates that each plot at a constant Ca or Ca' exhibits a similar upward convex property, although the hyperelastic

particles show a gradual decrease in r_e^* at $Re > 40$ only for cases with larger $Ca (\geq 0.02)$. For the hyperelastic particles with smaller Ca , r_e^* drops sharply at $Re \sim 40$ due to the transition of stable equilibrium position from the DEP to the MEP (see [figure 10a](#)). Additionally, both particles exhibit the trend that r_e^* at constant Re is smaller for larger Ca , implying that more deformable particles tend to focus closer to the channel centre.

For capsules in a confined square channel, Schaaf & Stark (2017) reported capsule migration behaviour in the same geometry. Although strict quantitative comparisons are not possible due to differences in the deformation metrics used to characterise particle stiffness (in terms of La and Ca), their results show behaviour broadly similar to our findings for viscous hyperelastic particles. As shown in figures 3(b) and 3(d) of Schaaf & Stark (2017), which correspond to our results at $Re \sim 5$ and 50, respectively, the changes in focusing patterns exhibit nearly the same trends. Capsules migrate towards the CEP at low La , and the focusing positions transition from the DEP to the MEP with increasing La . Regarding the migration velocity, a two-phase migration property is also observed, with softer capsules migrating faster, consistent with the elastic particle results in [figure 9](#). The primary difference lies in the bistable state between the DEP and MEP. This bistability is likely absent in the results of Schaaf & Stark (2017) because they computed trajectories from a single initial position, whereas capturing bistability requires simulations from at least two distinct initial positions. Another difference is the dependence of r_e^* and \mathcal{T} on La , shown in [figure 10\(b, c\)](#). Schaaf & Stark (2017) reported a critical Laplace number $La_c \sim 1$ for capsules with $\kappa = 0.2$ to move away from the CEP and noted that La_c changes sensitively with Re . In contrast, our results indicate $La_c \sim 8$ without clear dependence on Re within the low- Re regime as shown in [figure 10\(b\)](#). Additional details are provided in figures S2 and S3 in the Supplementary material.

In some cases in the present study, identifying the equilibrium position of the particle is very difficult, mainly due to their extremely slow migration in the second phase. This difficulty is unavoidable when the equilibrium position is determined from the calculation of trajectories. Instead of calculating trajectories, Schaaf & Stark (2017) estimated the lift exerted on a capsule by applying an adjustable force evenly distributed over all the membrane vertices to hold the capsule in place. By evaluating the external force to compensate the lift for various prescribed positions of the capsule, they obtained the lift map and determined the equilibrium position where the lift vanishes. In the present study, however, it is difficult to apply this method to the hyperelastic particles and thus to obtain the lift map.

3.3. Discussion of the stability of the channel centre

The phase diagram ([figure 10a](#)) suggests that the boundaries of focusing patterns appear to be formed along lines of constant La . Here, La is defined by the ratio of Re_p to Ca , indicating that both inertia (Re_p) and deformation (Ca) influence the transition of the focusing positions. This trend becomes even more apparent in the phase diagram plotted using (Re, La) coordinates, as shown in [figure S4](#) of the Supplementary material. In the following, we first explain why La serves as the characteristic scaling parameter for this phenomenon. Then, with the aid of additional numerical simulations, we present a semi-analytical discussion of the transition between CEP and DEP near the line of $La = 8$ using an asymptotic expansion of the forces acting on the particle, with Re_p and Ca as perturbed parameters.

3.3.1. Asymptotic expansion

Cox & Brenner (1968) applied matched asymptotic expansions to predict the migration of rigid spheres in Poiseuille flow with low Re . This approach was extended to include

inertial effects on the lateral migration of a neutrally buoyant rigid sphere in a Newtonian fluid, through an asymptotic expansion in terms of Re (Ho & Leal 1974; Hood, Lee & Roper 2015). For deformable drops, Chan & Leal (1979, 1981) applied perturbation methods and the reciprocal theorem to analyse deformation-induced migration. The effects of inertia and deformation on the lateral migration of bubbles near a wall were experimentally investigated by Takemura *et al.* (2002), and theoretically analysed by Magnaudet, Takagi & Legendre (2003) through a perturbation expansion in terms of the Galileo and Bond numbers. Sugiyama & Takemura (2010) also performed an asymptotic expansion in terms of Ca to analyse the lateral migration of slightly deformed bubbles rising near a wall, complementing the previous work by Magnaudet *et al.* (2003).

Using such an asymptotic expansion, the force acting on an slightly deformable sphere can be expressed as

$$\mathbf{F} = \mu d U f(y, z) \mathbf{e}_x - \mu d \mathbf{D} \cdot \mathbf{u} + Re_p \mu d U \mathbf{f}_I + Ca \mu d U \mathbf{f}_D + o(Re_p) + o(Ca). \quad (3.1)$$

The first and second terms represent the force on a rigid sphere in a creeping flow. The third and fourth terms correspond to the first-order terms of inertial lift and deformation-induced lift, respectively, expanded in terms of Re_p and Ca . Here, $f(y, z)$ is the force coefficient dependent on the cross-sectional position, \mathbf{D} is the drag coefficient matrix, and \mathbf{f}_I and \mathbf{f}_D are the dimensionless vectors representing the inertia and deformation-induced forces, respectively.

For small Re_p and Ca , the cross-sectional components (denoted by the \perp symbol) of the force can be expressed as

$$\mathbf{F}^\perp = -\mu d \mathbf{D}^\perp \cdot \mathbf{u}^\perp + Re_p \mu d U \mathbf{f}_I^\perp + Ca \mu d U \mathbf{f}_D^\perp. \quad (3.2)$$

The particle is at the equilibrium position, provided that

$$\mathbf{F}^\perp = \mathbf{0}, \quad \mathbf{u}^\perp = \mathbf{0}, \quad (3.3)$$

from which, (3.2) becomes

$$La \mathbf{f}_I^\perp + \mathbf{f}_D^\perp = \mathbf{0}, \quad (3.4)$$

where $La = Re_p/Ca$ is the Laplace number. Since \mathbf{f}_I and \mathbf{f}_D are functions of the cross-sectional coordinates and the blockage ratio κ , (3.4) indicates that La determines the particle's equilibrium positions. Once \mathbf{f}_I and \mathbf{f}_D are known, we may evaluate La at the equilibrium position. Subsequently, we shall demonstrate that (3.4) accounts for the change of the focusing pattern from the CEP to the DEP beyond $La \sim 8$ in figure 10(a). Upon decomposing (3.2) on the polar coordinates with the origin at the channel centre, we consider the following relation between the radial force F_r and velocity u_r of the particle near the origin:

$$F_r = -\mu d D_{rr} u_r + Re_p \mu d U f_{Ir} + Ca \mu d U f_{Dr}. \quad (3.5)$$

In § 3.3.2, we estimate f_{Ir} from numerical simulations for a rigid sphere ($Ca = 0$) at finite Re . In § 3.3.3, we estimate f_{Dr} from simulations for a hyperelastic particle (finite Ca) at $Re = 0$. In § 3.3.4, we examine the stability of the CEP.

3.3.2. Rigid sphere fixed within the cross-section

Di Carlo *et al.* (2009) computed the inertial lift force by simulating a fixed rigid particle within the cross-section using COMSOL Multi-physics. They expressed it in a dimensional form as $F_I = \rho U^2 d^2 \kappa f_I = \mu d U Re_p f_I$, where f_I is a function of the particle position. Nakagawa *et al.* (2015) also investigated the lateral migration of rigid spheres using the

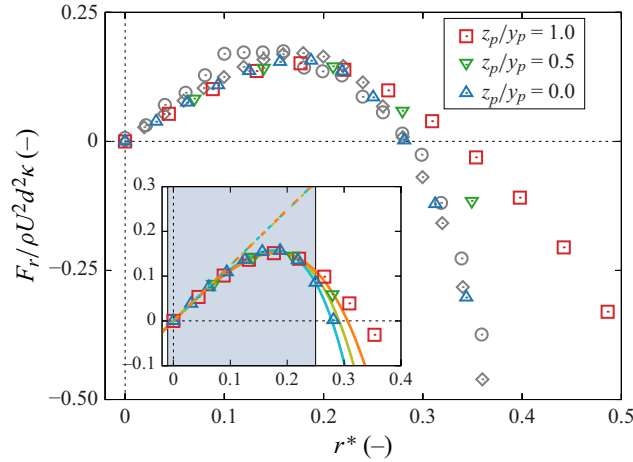


Figure 12. Force profile acting on a particle fixed at (y_p, z_p) with $Re = 40$, $Ca = 0$ and $\kappa = 0.22$, along three lines: (red squares) the midline $z_p/y_p = 0$, (green triangles) the diagonal line $z_p/y_p = 1.0$ and (blue triangles) the intermediate line $z_p/y_p = 0.5$. The case of $z_p/y_p = 0$ is compared with the previous studies: (grey circles) Di Carlo *et al.* (2009) and (grey diamonds) Nakagawa *et al.* (2015). (Inset) Fitting functions of a fifth-degree odd polynomial and linear fits with slopes of the first-degree coefficients.

immersed boundary method and clarified the stability of equilibrium positions through simulations of both fixed and moving particles. Following the approach of Nakagawa *et al.* (2015), we employ the immersed boundary method (detailed in Appendix A) for the numerical simulation of a rigid sphere, which freely moves in the streamwise direction and rotates in all the directions but rests at the cross-sectional position.

For a rigid sphere fixed within the cross-section ($u_r = 0$, $f_{Dr} = 0$), (3.5) becomes

$$F_r = Re_p \mu d U f_{Ir}. \quad (3.6)$$

Computing F_r along the straight lines across the centre within the cross-section, we estimate radial profiles of f_{Ir} based on (3.6), as shown in figure 12. Each coloured symbol represents the results along the midline ($z_p/y_p = 0$), the diagonal line ($z_p/y_p = 1.0$) and the intermediate line ($z_p/y_p = 0.5$), where (y_p, z_p) is the particle's centre of mass. The grey marks represent the results of Di Carlo *et al.* (2009) and Nakagawa *et al.* (2015) at $z_p/y_p = 0$, showing good agreements with the present results. We also simulated the moving particles and verified the particle motion towards the equilibrium point of $f_{Ir} = 0$. In all the cases, the particles near the channel centre migrated outwards, implying the instability of the CEP pattern as expected from figure 12. The solid lines represent odd polynomial fits (up to the fifth degree) of the discrete points near the origin ($0 \leq r^* \leq 0.25$). The dashed lines indicate linear fits with slopes a_1 corresponding to the first-order coefficients of the fitted functions. The force approximately increases along these linear lines, which are nearly identical. Thus, we obtain

$$f_{Ir} = \frac{F_r}{\rho U^2 d^2 \kappa} \approx a_1 r^*, \quad a_1 \approx (1.238 \pm 0.003) \text{ at } r^* \ll 1. \quad (3.7)$$

3.3.3. Deformable particle in Stokes flow

The deformation-induced force f_{Dr} in (3.5) is estimated by computing a hyperelastic particle moving in the Stokes flow. Assuming the quasi-steady motion of the particle (namely, $F_r = 0$) and employing Stokes's law ($D_{rr} = 3\pi$) in an infinite domain with

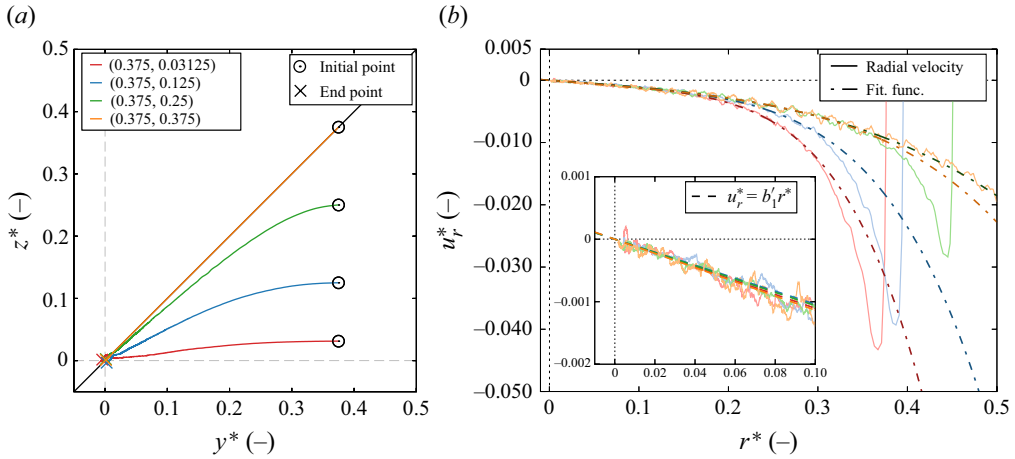


Figure 13. (a) Trajectories of the centroid of hyperelastic particles for $Re = 0$, $Ca = 0.01$ and $\kappa = 0.2$ with initial positions $y_0^* = 0.375$, $z_0^* = 0.03125, 0.125, 0.25, 0.375$. Circles indicate the initial positions, and crosses mark the end points of the calculation. (b) Velocity distributions of deformable particles in Stokes flow under the same conditions of panel (a). Dash-dotted lines indicate fifth-degree odd polynomial fits, while dotted lines represent linear approximations using the first-degree coefficients. The fitting range is $r^* \in [0 : 0.3]$.

$Re = 0$, (3.5) becomes

$$0 = -3\pi\mu du_r + Ca\mu dUf_{Dr}. \quad (3.8)$$

From (3.8), f_{Dr} is determined using the particle velocity u_r^* , namely

$$f_{Dr} = \frac{3\pi}{CaU} u_r = \frac{3\pi}{Ca} u_r^* \quad (\because u_r = Uu_r^*). \quad (3.9)$$

The distribution of u_r^* is found as the numerical solution to the equation set (2.2)–(2.5), where the left-hand side of (2.3) is omitted. The numerical simulations were conducted for seven initial positions given by $y_0^* = 0.375$, $z_0^* = 0.03125, 0.0625i$ ($i = 1, 2, \dots, 6$) and three capillary numbers $Ca = 0.005, 0.01, 0.015$. Figure 13 shows typical results of the particle trajectory and velocity. In all the cases, the particles migrate towards the channel centre, exhibiting the CEP pattern as expected (figure 13a). It is seen from the inset of figure 13(b) that the plots for different initial positions are likely to collapse onto a single line near the origin. By fitting the plots of u_r^* versus r^* with a fifth-order polynomial (odd polynomial up to degree 5) and approximating it near the centre ($r^* \ll 1$), the dimensionless velocity can be expressed as

$$u_r^* \approx b_1' r^*, \quad (3.10)$$

with $b_1' = 1.07 \times 10^{-2}$ for $Ca = 0.01$. The asymptotic expansion in § 3.3.1 supposes that f_{Dr} in (3.9) is independent of Ca and dependent only on r^* near the origin for given κ . Introducing $b_1 = b_1'/Ca$ gives

$$f_{Dr} = \frac{3\pi}{Ca} b_1' r^* = 3\pi b_1 r^*. \quad (3.11)$$

We find $b_1 = 1.07$ for $Ca = 0.01$, $b_1 = 0.863$ for $Ca = 0.005$, and $b_1 = 1.12$ for $Ca = 0.015$. Thus, b_1 remains nearly constant, specifically

$$b_1 = -(1.02 \pm 0.14). \quad (3.12)$$

3.3.4. Stability of CEP

Substituting (3.7) and (3.11) into (3.5) with $u_r = 0$ gives

$$F_r \approx Ca\mu dU (La a_1 r^* + 3\pi b_1 r^*). \quad (3.13)$$

Note that a_1 has a positive value, indicating that the inertial force drives the particle away from the channel centre, while b_1 has a negative value, resulting in the particle migrating towards the centre. Equations (3.3) and (3.13) indicate that the particle is at the equilibrium position if $r^* = 0$ or $La a_1 r^* + 3\pi b_1 r^* = 0$. Here, we consider a particle located slightly offset from the channel centre. In the case where $La a_1 r^* + 3\pi b_1 r^* < 0$, the radial force F_r is negative and, therefore, the particle migrates towards the centre $r^* = 0$, corresponding to the equilibrium position. By contrast, in the case where $La a_1 r^* + 3\pi b_1 r^* > 0$ (namely $F_r > 0$), the particle migrates away from the centre. Therefore, together with $F_r = 0$, we find the critical Laplace number La_c :

$$La_c = -\frac{3\pi b_1}{a_1} = 7.75 \pm 1.05, \quad (3.14)$$

beyond which the CEP pattern becomes unstable. This critical value in (3.14) shows a good agreement with the boundary at $La \sim 8$ in figure 10(a), indicating that the asymptotic expansion explains the transition of the particle focusing between the CEP and DEP regions.

4. Conclusions

In the present study, we used hydrogel microspheres as deformable particles to investigate experimentally the inertial migration of deformable particles flowing through square channels. The experiments have shown that at finite $Re (\geq 5)$, hydrogel particles with blockage ratio of 0.1 focus near four points located on the diagonals, which indicates the presence of stable equilibrium positions on the diagonal (DEP). As Re decreases, the particle focusing position moves inwards until the particles focus on the channel centre (CEP), i.e. axial accumulation, at low $Re (= 0.1)$. Corresponding numerical simulations using viscous hyperelastic particles predicted that Young's modulus of these hydrogel particles would be ~ 3.1 kPa, slightly smaller but comparable to extrapolations from previously reported values. Additionally, two-phase migration property observed for hydrogel particles was reproduced by the numerical simulation for hyperelastic particles at finite Re ; particles move rather quickly mostly in the radial direction towards the pSS ring in the first phase, followed by a slow migration along the pSS ring towards stable equilibrium positions in the second phase.

Furthermore, the numerical simulations for hyperelastic particles with a larger blockage ratio ($= 0.2$) showed that, as the particles become more deformable, their focusing pattern shifts from four-point focusing on the MEP (pattern C), to eight-point focusing on the MEP and DEP (pattern D), to four-point focusing on the DEP (pattern B), and to single-point focusing on the channel centre (pattern A). The particle focusing positions approach the channel centre with increasing particle deformability. These transitions of the particle focusing pattern can be accounted for by an increase in the particle deformation-induced lift, acting towards the lower shear.

In addition, we confirmed that the migration behaviour observed for hydrogel particles qualitatively agrees with previously reported capsule migration (Krüger *et al.* 2014b; Schaaf & Stark 2017). While quantitative comparison is complicated by differences in deformation metrics and particle models, key features such as the two-phase migration process and the transition of focusing patterns with particle deformability show

remarkable qualitative similarity. Notably, both studies observe particle focusing moving towards the channel centre with increasing deformability, and a corresponding variation in equilibrium positions depending on flow conditions. In the present study, we have constructed a phase diagram showing the particle focusing patterns as a function of Re and Ca (and Re and La in the Supplementary material).

Moreover, our study extends these findings by performing detailed stability analyses and theoretical modelling through asymptotic expansions with two perturbed parameters, Re_p and Ca , suggesting that the equilibrium position is governed by the balance between inertial lift and deformation-induced lift. Extra numerical simulations were performed to examine the stability of the CEP, and the predicted critical value from the theoretical analysis showed good agreement with the boundary of CEP and DEP regions in the phase diagram. The boundary between the DEP and MEP at high Re (or higher $La \sim 200$ in figure 10a) is difficult to analyse using asymptotic expansions, as the assumptions of small Re_p and Ca no longer hold. Additionally, further investigation is required to clarify why deformable particles tend to migrate towards the DEP at low Re , whereas rigid particles focus at the MEP under similar conditions. These two points/issues are beyond the scope of the present study and are left for future work.

Supplementary material. Supplementary material is available at <https://doi.org/10.1017/jfm.2025.10574>.

Funding. This research was partially supported by JSPS KAKENHI Grant Numbers JP20H02072, and JP24K00809. YH was supported by JST SPRING, Grant Number JPMJSP2138. Part of the results was obtained by supercomputer Fugaku at the RIKEN R-CCS through the HPCI System Research Project (Project ID: hp220106), SQUID at D3 centre, Osaka University, and GENKAI at Research Institute for Information Technology, Kyushu University.

Declaration of interests. The authors report no conflict of interest.

Appendix A.

The numerical simulations of neutrally buoyant rigid particle were conducted using the immersed boundary method (IBM) based on Kajishima *et al.* (2001). The rigid density is the same as the fluid one. Here, we will outline the numerical algorithm applicable only when the particle is spherical and the density ρ is spatially uniform and time-invariant.

The governing equations are

$$\nabla \cdot \mathbf{u} = 0, \quad (\text{A1})$$

$$\rho \frac{D\mathbf{u}}{Dt} = \nabla \cdot \boldsymbol{\sigma} + \mathbf{f}_p, \quad (\text{A2})$$

where $D/Dt = \partial/\partial t + \mathbf{u} \cdot \nabla$ is the material derivative, and \mathbf{f}_p is the body force for coupling the rigid and fluid motions. Note that although we use the method to fix the x -coordinate of the particle centroid in the computational space as described in § 2.3, we here write equations of the physical space in the inertial coordinates (where the particle freely moves) for simplicity of explanation. Additionally, the stress tensor $\boldsymbol{\sigma}$ includes the influence of driving pressure dp/dx_{drive} . The IBM consists of two sequential procedures in the progression from the n th time step to the $(n+1)$ th one.

In the first procedure, the entire domain is regarded as a fluid. To satisfy (A1) and (A2) with $\mathbf{f}_p = 0$, the velocity $\tilde{\mathbf{u}}$ is found by the SMAC algorithm

$$\begin{aligned} \tilde{\mathbf{u}} = \mathbf{u}^n + \Delta t \left(-\frac{3}{2}(\mathbf{u} \cdot \nabla \mathbf{u})^n + \frac{1}{2}(\mathbf{u} \cdot \nabla \mathbf{u})^{n-1} - \frac{1}{\rho} \nabla p^n \right. \\ \left. + \frac{1}{\rho} \left\{ \frac{3}{2}(\nabla \cdot \boldsymbol{\sigma}')^n - \frac{1}{2}(\nabla \cdot \boldsymbol{\sigma}')^{n-1} \right\} \right), \end{aligned} \quad (\text{A3})$$

$$\nabla^2 \delta p = \frac{\rho}{\Delta t} \nabla \cdot \tilde{\mathbf{u}}, \quad (\text{A4})$$

$$\hat{\mathbf{u}} = \tilde{\mathbf{u}} - \frac{\Delta t}{\rho} \nabla \delta p, \quad (\text{A5})$$

where $\tilde{\mathbf{u}}$ is the unprojection velocity, $\delta p = p^{n+1} - p^n$ is the pressure increment and $\boldsymbol{\sigma}' = \boldsymbol{\sigma} - \text{tr}(\boldsymbol{\sigma})\mathbf{I}/3$ is the deviatoric stress tensor. In (A3), the second-order Adams–Bashforth (AB2) scheme is applied to $\mathbf{u} \cdot \nabla \mathbf{u}$ and $\nabla \cdot \boldsymbol{\sigma}'$.

In the second procedure, the rigid and fluid motions are coupled. The AB2 scheme updates the particle centroid position \mathbf{x}_p in a way,

$$\mathbf{x}_p^{n+1} = \mathbf{x}_p^n + \Delta t \left(\frac{3}{2} \mathbf{v}_p^n - \frac{1}{2} \mathbf{v}_p^{n-1} \right), \quad (\text{A6})$$

where \mathbf{v}_p denotes the translational velocity of the particle. To have the same smoothness across the interface as the present fluid–structure interaction simulation (see § 2.3), the rigid volume fraction α at the location \mathbf{x} is given by

$$\alpha = \frac{1}{2} \left(1 - \tanh \frac{\beta(|\mathbf{r}_p| - d/2)}{\Delta x} \right), \quad (\text{A7})$$

where $\mathbf{r}_p = \mathbf{x} - \mathbf{x}_p$ is the relative position vector to the particle centroid, d is the sphere diameter and $\beta(=2)$ is the sharpness parameter relative to the grid width Δx . From (A2)–(A5), \mathbf{u}^{n+1} is determined as

$$\mathbf{u}^{n+1} = \hat{\mathbf{u}} + \frac{\Delta t}{\rho} \mathbf{f}_p. \quad (\text{A8})$$

To impose the rigid motion inside the particle, the coupling force \mathbf{f}_p in (A8) is

$$\mathbf{f}_p = \alpha^{n+1} \rho \frac{\mathbf{u}_p^{n+1} - \hat{\mathbf{u}}}{\Delta t}, \quad (\text{A9})$$

where \mathbf{u}_p^{n+1} is the particle velocity at the $(n+1)$ th time step given by

$$\mathbf{u}_p^{n+1} = \mathbf{v}_p^{n+1} + \boldsymbol{\omega}_p^{n+1} \times \mathbf{r}_p^{n+1}, \quad (\text{A10})$$

where $\boldsymbol{\omega}_p$ denotes the rotational velocity of the particle. In the subsequent development, we will clarify how to identify \mathbf{v}_p^{n+1} and $\boldsymbol{\omega}_p^{n+1}$. The equations of motion for the spherical particle are

$$m_p \frac{d\mathbf{v}_p}{dt} = \oint_{S_p} \mathbf{n}_p \cdot \boldsymbol{\sigma} dS, \quad (\text{A11})$$

$$\mathbf{I}_p \cdot \frac{d\boldsymbol{\omega}_p}{dt} = \oint_{S_p} \mathbf{r}_p \times (\mathbf{n}_p \cdot \boldsymbol{\sigma}) dS, \quad (\text{A12})$$

where $m_p(=\pi\rho d^3/6)$ is the particle mass, S_p is the particle surface, \mathbf{n}_p is the outward unit normal vector on the surface and $\mathbf{I}_p(=\pi\rho d^5\mathbf{I}/60)$ is the inertia tensor. As long as the grid resolution is sufficiently fine, the rigid volume fraction α possesses the nature of the Heaviside function, and thus m_p and \mathbf{v}_p may be written as

$$m_p = \rho \int_V \alpha dV, \quad \mathbf{v}_p = \frac{\int_V \alpha \mathbf{u} dV}{\int_V \alpha dV} = \frac{\int_V \alpha \mathbf{u}_p dV}{\int_V \alpha dV}, \quad (\text{A13})$$

where V is the volume of the entire domain. To be treated in the IBM, (A11) is approximated with the grid scale smoothness. Introducing a smoothed delta function $\delta = |\nabla\alpha|$, which is non-zero only near the interface, we express the normal vector \mathbf{n}_p and the surface integral as

$$\mathbf{n}_p = -\frac{\nabla\alpha}{\delta}, \quad \oint_{S_p} \dots dS = \int_V \dots \delta dV. \quad (\text{A14})$$

From (A14), an arbitrary tensor \mathbf{T} satisfies

$$\oint_{S_p} \mathbf{n}_p \cdot \mathbf{T} dS = - \int_V \nabla\alpha \cdot \mathbf{T} dV = - \int_V \nabla \cdot (\alpha\mathbf{T}) dV + \int_V \alpha \nabla \cdot \mathbf{T} dV. \quad (\text{A15})$$

Applying the divergence theorem to the first term on the right-hand side of (A15) gives

$$\int_V \nabla \cdot (\alpha\mathbf{T}) dV = \oint_{\partial V} \mathbf{n} \cdot (\alpha\mathbf{T}) dS = 0. \quad (\text{A16})$$

Here, we supposed no particle (i.e. $\alpha = 0$) on the boundary ∂V of the entire domain. From (A2), (A15) and (A16), the right-hand side of (A11) is rewritten in a volume integral form

$$\oint_{S_p} \mathbf{n}_p \cdot \boldsymbol{\sigma} dS = \int_V \alpha \nabla \cdot \boldsymbol{\sigma} dV = \int_V \alpha \rho \frac{D\mathbf{u}}{Dt} dV - \int_V \alpha \mathbf{f}_p dV. \quad (\text{A17})$$

Using the conservation of the volume fraction $D\alpha/Dt = 0$ and the Lagrangian time derivative $d/dt = \partial/\partial t + \mathbf{v}_p \cdot \nabla$ along the particle centroid together with (A1), the first term on the right-hand side of (A17) becomes

$$\int_V \alpha \rho \frac{D\mathbf{u}}{Dt} dV = \rho \int_V \frac{d(\alpha\mathbf{u})}{dt} dV + \underbrace{\rho \int_V \nabla \cdot (\alpha(\mathbf{u} - \mathbf{v}_p)\mathbf{u}) dV}_{=0}. \quad (\text{A18})$$

On the right-hand side of (A18), the first term may be written as

$$\rho \int_V \frac{d(\alpha\mathbf{u})}{dt} dV = \rho \frac{d}{dt} \int_V \alpha\mathbf{u} dV \quad (\text{A19})$$

owing to the time-invariance of the domain in the inertial coordinates. Further, the second term vanishes because of (A16). The relations $\mathbf{f}_p \neq 0$ and $\alpha = 1$ are valid only inside the particle. Therefore, the translational motion equation (A11) with (A13) and (A17)–(A19) reduces into

$$\int_V \mathbf{f}_p dV = 0. \quad (\text{A20})$$

From (A9), (A13) and (A20), we arrive at the expression of the translational velocity at the $(n+1)$ th time step

$$\mathbf{v}_p^{n+1} = \frac{\int_V \alpha^{n+1} \mathbf{u}_p^{n+1} dV}{\int_V \alpha^{n+1} dV} = \frac{\int_V \alpha^{n+1} \hat{\mathbf{u}} dV}{\int_V \alpha^{n+1} dV}. \quad (\text{A21})$$

Through a similar process to the derivation of (A20), the rotational motion equation (A12) reduces into

$$\int_V \mathbf{r}_p^{n+1} \times \mathbf{f}_p dV = 0. \quad (\text{A22})$$

From (A9), (A10) and (A22), we can express the i th component of the rotational velocity at the $(n + 1)$ th time step in Einstein's index notation

$$\omega_{p,i}^{n+1} = \frac{\int_V \alpha^{n+1} (\varepsilon_{ijk} r_{p,j}^{n+1} \hat{u}_k) dV}{\int_V \alpha^{n+1} (|\mathbf{r}_p^{n+1}|^2 - (r_{p,i}^{n+1})^2) dV} \quad (\text{no sum. with respect to } i), \quad (\text{A23})$$

where ε_{ijk} denotes the Levi-Civita symbol. The expressions (A10), (A21) and (A23) indicate that the velocity \mathbf{u}_p^{n+1} of the neutrally buoyant particle depends only on $\hat{\mathbf{u}}$, \mathbf{x}_p^{n+1} and α^{n+1} (which are given by (A5), (A6) and (A7), respectively), and is identified without time-integral operation for \mathbf{v}_p and $\boldsymbol{\omega}_p$. Once these quantities are known, we can determine the coupling force \mathbf{f}_p by (A9) and update \mathbf{u}^{n+1} by (A8).

In the numerical simulation with the rigid sphere fixed within the cross-section in § 3.3.2, the particle obeys (A22) and freely rotates. Further, it freely translates in the x -direction despite $\mathbf{e}_y \cdot \mathbf{v}_p = 0$ and $\mathbf{e}_z \cdot \mathbf{v}_p = 0$. For such a translational motion, the reduced equation is

$$\mathbf{e}_x \cdot \int_V \mathbf{f}_p dV = 0. \quad (\text{A24})$$

Thus, \mathbf{x}_p^{n+1} , α^{n+1} , \mathbf{v}_p^{n+1} , $\boldsymbol{\omega}_p^{n+1}$, \mathbf{f}_p and \mathbf{u}^{n+1} are determined in the above-mentioned manner except that (A21) is replaced with

$$\mathbf{v}_p^{n+1} = \mathbf{e}_x \frac{\int_V \alpha^{n+1} \mathbf{e}_x \cdot \hat{\mathbf{u}} dV}{\int_V \alpha^{n+1} dV}. \quad (\text{A25})$$

In the steady state with $d\mathbf{v}_p/dt = 0$, from (A13), (A17)–(A19) and (A24), we may estimate the cross-sectional force \mathbf{F}^\perp (see § 3.3.2) as

$$\mathbf{F}^\perp = \mathbf{P}^\perp \cdot \oint_{S_p} \mathbf{n}_p \cdot \boldsymbol{\sigma} dS = -\mathbf{P}^\perp \cdot \int_V \mathbf{f}_p dV = - \int_V \mathbf{f}_p dV, \quad (\text{A26})$$

where $\mathbf{P}^\perp = \mathbf{I} - \mathbf{e}_x \mathbf{e}_x$ is the projection tensor onto the cross-section.

REFERENCES

- ABBAS, M., MAGAUD, P., GAO, Y. & GEOFFROY, S. 2014 Migration of finite sized particles in a laminar square channel flow from low to high Reynolds numbers. *Phys. Fluids* **26** (12), 123301.
- AMSDEN, A.A. & HARLOW, F.H. 1970 A simplified MAC technique for incompressible fluid flow calculations. *J. Comput. Phys.* **6** (2), 322–325.
- ASMOLOV, E.S. 1999 The inertial lift on a spherical particle in a plane Poiseuille flow at large channel Reynolds number. *J. Fluid Mech.* **381**, 63–87.
- BANQUY, X., SUAREZ, F., ARGAW, A., RABANEL, J.-M., GRUTTER, P., BOUCHARD, J.-F., HILDGEN, P. & GIASSON, S. 2009 Effect of mechanical properties of hydrogel nanoparticles on macrophage cell uptake. *Soft Matt.* **5** (20), 3984–3991.
- BHAGAT, A.A.S., BOW, H., HOU, H.W., TAN, S.J., HAN, J. & LIM, C.T. 2010 Microfluidics for cell separation. *Med. Biol. Engng Comput.* **48**, 999–1014.
- BHAGAT, A.A.S., KUNTAEGOWDANAHALLI, S.S. & PAPAUTSKY, I. 2008 Enhanced particle filtration in straight microchannels using shear-modulated inertial migration. *Phys. Fluids* **20** (10), 101702.
- BONET, J. & WOOD, R.D. 2008 *Nonlinear Continuum Mechanics for Finite Element Analysis*. Cambridge University Press.
- CANUTO, C., HUSSAINI, M.Y., QUARTERONI, A. & ZANG, T.A. 2012 *Spectral Methods in Fluid Dynamics*. Springer Science & Business Media.
- CHAN, P.C.-H. & LEAL, L.G. 1981 An experimental study of drop migration in shear flow between concentric cylinders. *Intl J. Multiphase Flow* **7** (1), 83–99.
- CHAN, P.C.-H. & LEAL, L.G. 1979 The motion of a deformable drop in a second-order fluid. *J. Fluid Mech.* **92** (1), 131–170.

- CHOI, Y.-S., SEO, K.-W. & LEE, S.-J. 2011 Lateral and cross-lateral focusing of spherical particles in a square microchannel. *Lab on a Chip* **11** (3), 460–465.
- CHUN, B. & LADD, A.J.C. 2006 Inertial migration of neutrally buoyant particles in a square duct: an investigation of multiple equilibrium positions. *Phys. Fluids* **18** (3), 031704.
- CONNOLLY, S., MCGOURTY, K. & NEWPORT, D. 2021 The influence of cell elastic modulus on inertial positions in Poiseuille microflows. *Biophys. J.* **120** (5), 855–865.
- CORNISH, R.J. 1928 Flow in a pipe of rectangular cross-section. *Proc. R. Soc. Lond. A* **120** (786), 691–700.
- COX, R.G. & BRENNER, H. 1968 The lateral migration of solid particles in Poiseuille flow – I theory. *Chem. Engng Sci.* **23** (2), 147–173.
- DI CARLO, D. 2009 Inertial microfluidics. *Lab on a Chip* **9** (21), 3038–3046.
- DI CARLO, D., EDD, J.F., HUMPHRY, K.J., STONE, H.A. & TONER, M. 2009 Particle segregation and dynamics in confined flows. *Phys. Rev. Lett.* **102**, 094503.
- DI CARLO, D., IRIMIA, D., TOMPKINS, R.G. & TONER, M. 2007 Continuous inertial focusing, ordering, and separation of particles in microchannels. *Proc. Natl. Acad. Sci. USA* **104** (48), 18892–18897.
- DING, Z., XIAO, Y., ZHANG, H., ZHANG, K., ZHU, C., WANG, L.-P. & XUE, Y. 2025 Deformation and focusing of hydrogel microparticles in microfluidic flow: mimicking the segregation of cancer cells with similar sizes. *J. Fluid Mech.* **1007**, A85.
- ESPOSITO, G., ROMANO, S., HULSEN, M.A., D’AVINO, G. & VILLONE, M.M. 2022 Numerical simulations of cell sorting through inertial microfluidics. *Phys. Fluids* **34** (7), 072009.
- ESTEGHAMATIAN, A., KATZ, J. & ZAKI, T.A. 2022 Spatiotemporal characterization of turbulent channel flow with a hyperelastic compliant wall. *J. Fluid Mech.* **942**, A35.
- GERZ, T., SCHUMANN, U. & ELGHOBASHI, S.E. 1989 Direct numerical simulation of stratified homogeneous turbulent shear flows. *J. Fluid Mech.* **200**, 563–594.
- GOLDSMITH, H.L. 1971 Red cell motions and wall interactions in tube flow. *Federation Proc.* **30** (5), 1578–1590.
- GUO, Q., DUFFY, S.P., MATTHEWS, K., ISLAMZADA, E. & MA, H.A.-O. 2017 Deformability based cell sorting using microfluidic ratchets enabling phenotypic separation of leukocytes directly from whole blood. *Sci. Rep.* **7** (1), 6627.
- HIRT, C.W. & NICHOLS, B.D. 1981 Volume of fluid (VOF) method for the dynamics of free boundaries. *J. Comput. Phys.* **39** (1), 201–225.
- HO, B.P. & LEAL, L.G. 1974 Inertial migration of rigid spheres in two-dimensional unidirectional flows. *J. Fluid Mech.* **65** (2), 365–400.
- HOCHMUTH, R.M. 1987 Properties of red blood cells. In *Handbook of Bioengineering* (ed. R. Skalak & S. Chien), pp. chap. 12, McGraw-Hill.
- HODGES, S.R., JENSEN, O.E. & RALLISON, J.M. 2004 Sliding, slipping and rolling: the sedimentation of a viscous drop down a gently inclined plane. *J. Fluid Mech.* **512**, 95–131.
- HOLMES, D., WHYTE, G., BAILEY, J., VERGARA-IRIGARAY, N., EKPENYONG, A., GUCK, J. & DUKE, T. 2014 Separation of blood cells with differing deformability using deterministic lateral displacement. *Interface Focus* **4** (6), 20140011.
- HOOD, K., LEE, S. & ROPER, M. 2015 Inertial migration of a rigid sphere in three-dimensional Poiseuille flow. *J. Fluid Mech.* **765**, 452–479.
- VAN HOOGSTRAAT, P.A.A., SLAATS, P.M.A. & BAAIJENS, F.P.T. 1994 A Eulerian approach to the finite element modelling of neo-Hookean rubber material. *Appl. Sci. Res.* **48** (2), 193–210.
- HOU, H.W., BHAGAT, A.A.S., CHONG, A.G.L., MAO, P., TAN, K.S.W., HAN, J. & LIM, C.T. 2010 Deformability based cell margination – a simple microfluidic design for malaria-infected erythrocyte separation. *Lab on a Chip* **10** (19), 2605–2613.
- HUR, S.C., HENDERSON-MACLENNAN, N.K., MCCABE, E.R.B. & DI CARLO, D. 2011 Deformability-based cell classification and enrichment using inertial microfluidics. *Lab on a Chip* **11** (5), 912–920.
- II, S., GONG, X., SUGIYAMA, K., WU, J., HUANG, H. & TAKAGI, S. 2012a A full Eulerian fluid-membrane coupling method with a smoothed volume-of-fluid approach. *Commun. Comput. Phys.* **12** (2), 544–576.
- II, S., SUGIYAMA, K., TAKEUCHI, S., TAKAGI, S., MATSUMOTO, Y. & XIAO, F. 2012b An interface capturing method with a continuous function: the THINC method with multi-dimensional reconstruction. *J. Comput. Phys.* **231** (5), 2328–2358.
- JIANG, G.-S. & SHU, C.-W. 1996 Efficient implementation of weighted ENO schemes. *J. Comput. Phys.* **126** (1), 202–228.
- KAJISHIMA, T. & TAIRA, K. 2016 *Computational Fluid Dynamics: Incompressible Turbulent Flows*. Springer.
- KAJISHIMA, T., TAKIGUCHI, S., HAMASAKI, H. & MIYAKE, Y. 2001 Turbulence structure of particle-laden flow in a vertical plane channel due to vortex shedding. *JSME Intl J. Ser. B Fluids Therm. Engng* **44** (4), 526–535.

- KALYAN, S., TORABI, C., KHOO, H., SUNG, H.W., CHOI, S.-E., WANG, W., TREUTLER, B., KIM, D. & HUR, S.C. 2021 Inertial microfluidics enabling clinical research. *Micromachines* **12** (3).
- KAOU, B., RISTOW, G.H., CANTAT, I., MISBAH, C. & ZIMMERMANN, W. 2008 Lateral migration of a two-dimensional vesicle in unbounded Poiseuille flow. *Phys. Rev. E* **77**, 021903.
- KARIMI, A., YAZDI, S. & ARDEKANI, A.M. 2013 Hydrodynamic mechanisms of cell and particle trapping in microfluidics. *Biomechanics* **7** (2), 021501.
- KARNIS, A., GOLDSMITH, H.L. & MASON, S.G. 1963 Axial migration of particles in Poiseuille flow. *Nature* **200** (4902), 159–160.
- KAWAMOTO, T., MINATO, H. & SUZUKI, D. 2024 Relationship between π – A isotherms and single microgel/microgel array structures revealed via the direct visualization of microgels at the air/water interface. *Soft Matt.* **20** (29), 5836–5847.
- KAWAMOTO, T., YANAGI, K., NISHIZAWA, Y., MINATO, H. & SUZUKI, D. 2023 The compression of deformed microgels at an air/water interface. *Chem. Commun.* **59** (89), 13289–13292.
- KRÜGER, T., HOLMES, D. & COVENEY, P.V. 2014a Deformability-based red blood cell separation in deterministic lateral displacement devices – a simulation study. *Biomechanics* **8** (5), 054114.
- KRÜGER, T., KAOU, B. & HARTING, J. 2014b Interplay of inertia and deformability on rheological properties of a suspension of capsules. *J. Fluid Mech.* **751**, 725–745.
- LEAL, L.G. 1980 Particle motions in a viscous fluid. *Annu. Rev. Fluid Mech.* **12**, 435–476.
- LEE, S., KIM, H. & YANG, S. 2023 Microfluidic label-free hydrodynamic separation of blood cells: recent developments and future perspectives. *Adv. Mater. Technol.* **8** (9), 2201425.
- LIU, X.-D., OSHER, S. & CHAN, T. 1994 Weighted essentially non-oscillatory schemes. *J. Comput. Phys.* **115** (1), 200–212.
- LOSSERAND, S., COUPIER, G. & PODGORSKI, T. 2019 Migration velocity of red blood cells in microchannels. *Microvasc. Res.* **124**, 30–36.
- MAGNAUDET, J., TAKAGI, S. & LEGENDRE, D. 2003 Drag, deformation and lateral migration of a buoyant drop moving near a wall. *J. Fluid Mech.* **476**, 115–157.
- MARTEL, J.M. & TONER, M. 2014 Inertial focusing in microfluidics. *Annu. Rev. Biomed. Engng* **16** (1), 371–396.
- MATAS, J.-P., MORRIS, J.F. & GUZZELLI, E. 2004 Lateral forces on a sphere. *Oil Gas Sci. Technol.* **59** (1), 59–70.
- MATAS, J.-P., MORRIS, J.F. & GUZZELLI, E. 2009 Lateral force on a rigid sphere in large-inertia laminar pipe flow. *J. Fluid Mech.* **621**, 59–67.
- MCFAUL, S.M., LIN, B.K. & MA, H. 2012 Cell separation based on size and deformability using microfluidic funnel ratchets. *Lab on a Chip* **12** (13), 2369–2376.
- MCHEDLISHVILI, G. & MAEDA, N. 2001 Blood flow structure related to red cell flow: determinant of blood fluidity in narrow microvessels. *Jpn. J. Physiol.* **51** (1), 19–30.
- MINATO, H., MURAI, M., WATANABE, T., MATSUI, S., TAKIZAWA, M., KUREHA, T. & SUZUKI, D. 2018 The deformation of hydrogel microspheres at the air/water interface. *Chem. Commun.* **54** (8), 932–935.
- MISBAH, C. 2014 Soft suspensions: inertia cooperates with flexibility. *J. Fluid Mech.* **760**, 1–4.
- MIURA, K., ITANO, T. & SUGIHARA-SEKI, M. 2014 Inertial migration of neutrally buoyant spheres in a pressure-driven flow through square channels. *J. Fluid Mech.* **749**, 320–330.
- MOONEY, M. 1940 A theory of large elastic deformation. *J. Appl. Phys.* **11** (9), 582–592.
- MORTAZAVI, S. & TRYGGVASON, G. 2000 A numerical study of the motion of drops in Poiseuille flow. Part 1. Lateral migration of one drop. *J. Fluid Mech.* **411**, 325–350.
- NAKAGAWA, N., YABU, T., OTOMO, R., KASE, A., MAKINO, M., ITANO, T. & SUGIHARA-SEKI, M. 2015 Inertial migration of a spherical particle in laminar square channel flows from low to high Reynolds numbers. *J. Fluid Mech.* **779**, 776–793.
- PARK, E.S. *et al.* 2016 Continuous flow deformability-based separation of circulating tumor cells using microfluidic ratchets. *Small* **12** (14), 1909–1919.
- PRASAD, V., SHARMA, A. & KULKARNI, S.S. 2022 Lid-driven cavity flow-induced dynamics of a neutrally buoyant solid: effect of Reynolds number, flexibility, and size. *Phys. Fluids* **34** (7), 073310.
- PREIRA, P., GRANDNE, V., FOREL, J.-M., GABRIELE, S., CAMARA, M. & THEODOLY, O. 2013 Passive circulating cell sorting by deformability using a microfluidic gradual filter. *Lab on a Chip* **13** (1), 161–170.
- RAFFIEE, A.H., DABIRI, S. & ARDEKANI, A.M. 2017 Elasto-inertial migration of deformable capsules in a microchannel. *Biomechanics* **11** (6), 064113.
- RAMANUJAN, S. & POZRIKIDIS, C. 1998 Deformation of liquid capsules enclosed by elastic membranes in simple shear flow: large deformations and the effect of fluid viscosities. *J. Fluid Mech.* **361**, 117–143.
- RAZAVI BAZAZ, S., MASHHADIAN, A., EHSANI, A., SAHA, S.C., KRÜGER, T. & EBRAHIMI WARKIANI, M. 2020 Computational inertial microfluidics: a review. *Lab on a Chip* **20** (6), 1023–1048.

- REZGHI, A., LI, P. & ZHANG, J. 2022 Lateral migration of viscoelastic capsules in tube flow. *Phys. Fluids* **34** (1), 011906.
- RIVLIN, R.S. 1948 Large elastic deformations of isotropic materials IV. Further developments of the general theory. *Phil. Trans. R. Soc. Lond. A* **241** (835), 379–397.
- ROSTI, M.E. & BRANDT, L. 2017 Numerical simulation of turbulent channel flow over a viscous hyper-elastic wall. *J. Fluid Mech.* **830**, 708–735.
- ROSTI, M.E. & BRANDT, L. 2018 Suspensions of deformable particles in a Couette flow. *J. Non-Newtonian Fluid Mech.* **262**, 3–11.
- ROSTI, M.E., BRANDT, L. & MITRA, D. 2018 Rheology of suspensions of viscoelastic spheres: deformability as an effective volume fraction. *Phys. Rev. Fluids* **3** (1), 012301.
- SASAKI, T., SEKI, J., ITANO, T. & SUGIHARA-SEKI, M. 2017 Cross-sectional distributions of normal and abnormal red blood cells in capillary tubes determined by a new technique. *Biorheology* **54** (5-6), 153–165.
- SCHAAF, C. & STARK, H. 2017 Inertial migration and axial control of deformable capsules. *Soft Matt.* **13** (19), 3544–3555.
- SCHONBERG, J.A. & HINCH, E.J. 1989 Inertial migration of a sphere in Poiseuille flow. *J. Fluid Mech.* **203**, 517–524.
- SEGRÉ, G. & SILBERBERG, A. 1961 Radial particle displacements in Poiseuille flow of suspensions. *Nature* **189**, 209–210.
- SEGRÉ, G. & SILBERBERG, A. 1962 Behaviour of macroscopic rigid spheres in Poiseuille flow part 2. Experimental results and interpretation. *J. Fluid Mech.* **14**, 136–157.
- SEKIMOTO, K. & LEIBLER, L. 1993 A mechanism for shear thickening of polymer-bearing surfaces: elasto-hydrodynamic coupling. *Europhys. Lett.* **23** (2), 113.
- SHICHI, H., YAMASHITA, H., SEKI, J., ITANO, T. & SUGIHARA-SEKI, M. 2017 Inertial migration regimes of spherical particles suspended in square tube flows. *Phys. Rev. Fluids* **2**, 044201.
- SHIN, S.J. & SUNG, H.J. 2011 Inertial migration of an elastic capsule in a Poiseuille flow. *Phys. Rev. E* **83**, 046321.
- STATHOULOPOULOS, A., PASSOS, A., KALIVIOTIS, E. & BALABANI, S. 2024 Partitioning of dense RBC suspensions in single microfluidic bifurcations: role of cell deformability and bifurcation angle. *Sci. Rep.* **14** (1), 535.
- STOECKLEIN, D. & DI CARLO, D. 2019 Nonlinear microfluidics. *Anal. Chem.* **91** (1), 296–314.
- SUGIYAMA, K., II, S., TAKEUCHI, S., TAKAGI, S. & MATSUMOTO, Y. 2011 A full Eulerian finite difference approach for solving fluid-structure coupling problems. *J. Comput. Phys.* **230**, 596–627.
- SUGIYAMA, K. & TAKEMURA, F. 2010 On the lateral migration of a slightly deformed bubble rising near a vertical plane wall. *J. Fluid Mech.* **662**, 209–231.
- TAKEISHI, N., ISHIMOTO, K., YOKOYAMA, N. & ROSTI, M.E. 2025 Inertial focusing of spherical capsule in pulsatile channel flows. *J. Fluid Mech.* **1008**, A46.
- TAKEISHI, N., ROSTI, M.E., IMAI, Y., WADA, S. & BRANDT, L. 2019 Haemorheology in dilute, semi-dilute and dense suspensions of red blood cells. *J. Fluid Mech.* **872**, 818–848.
- TAKEMURA, F., MAGNAUDET, J. & DIMITRAKOPOULOS, P. 2009 Migration and deformation of bubbles rising in a wall-bounded shear flow at finite Reynolds number. *J. Fluid Mech.* **634**, 463–486.
- TAKEMURA, F., TAKAGI, S., MAGNAUDET, J. & MATSUMOTO, Y. 2002 Drag and lift forces on a bubble rising near a vertical wall in a viscous liquid. *J. Fluid Mech.* **461**, 277–300.
- TANAKA, S. & SUGIHARA-SEKI, M. 2022 Inertial focusing of red blood cells suspended in square capillary tube flows. *J. Phys. Soc. Jpn.* **91** (8), 083401.
- TANG, W., ZHU, S., JIANG, D., ZHU, L., YANG, J. & XIANG, N. 2020 Channel innovations for inertial microfluidics. *Lab on a Chip* **20** (19), 3485–3502.
- TAYLOR, G.I. 1934 The formation of emulsions in definable fields of flow. *Proc. R. Soc. Lond. A* **146** (858), 501–523.
- VILLONE, M.M. 2019 Lateral migration of deformable particles in microfluidic channel flow of Newtonian and viscoelastic media: a computational study. *Microfluid. Nanofluid.* **23** (3), 47.
- VILLONE, M.M., GRECO, F., HULSEN, M.A. & MAFFETTONE, P.L. 2016 Numerical simulations of deformable particle lateral migration in tube flow of Newtonian and viscoelastic media. *J. Non-Newtonian Fluid Mech.* **234**, 105–113.
- VILLONE, M.M. & MAFFETTONE, P.L. 2019 Dynamics, rheology, and applications of elastic deformable particle suspensions: a review. *Rheol. Acta* **58**, 109–130.
- WANG, G., MAO, W., BYLER, R., PATEL, K., HENEGAR, C., ALEXEEV, A. & SULCHEK, T. 2013 Stiffness dependent separation of cells in a microfluidic device. *PLOS ONE* **8** (10), e75901.

- YANG, S., LEE, S.S., AHN, S.W., KANG, K., SHIM, W., LEE, G., HYUN, K. & KIM, J.M. 2012 Deformability-selective particle entrainment and separation in a rectangular microchannel using medium viscoelasticity. *Soft Matt.* **8** (18), 5011–5019.
- ZHANG, T. *et al.* 2024 Passive microfluidic devices for cell separation. *Biotechnol. Adv.* **71**, 108317.
- ZHOU, J. & PAPAUTSKY, I. 2013 Fundamentals of inertial focusing in microchannels. *Lab on a Chip* **13** (6), 1121–1132.